Numerical analysis and simulation of graphene assisted silicon-nitride waveguide

by

Amirhossein Hajbagheri

A thesis

presented to the University of Waterloo

in fulfillment of the

thesis requirement for the degree of

Master of science

in

Electrical Computer Engineering

Waterloo, Ontario, Canada, 2021

© Amirhossein Hajbagheri 2021

Author's Declaration

I hereby declare that I am the sole author of this thesis. This is a true copy of the thesis, including any required final revisions, as accepted by my examiners.

I understand that my thesis may be made electronically available to the public.

Abstract

To address the increased demand for high performance nonlinear integrated photonic devices, this thesis investigates a potential solution to the intrinsic low nonlinear response of silicon nitride waveguides by integrating a layer of graphene with the silicon-nitride. This thesis represents a simulation, analyze and design of graphene integrated silicon-nitride waveguide. To study the effect of this extra layer, a detailed simulation is performed using the finite difference time domain (FDTD) method, and the results are compared with those of the commercial software Lumerical FDTD.

The two methods produce results that strongly agree with each other, and show that the Kerr nonlinear response of silicon-nitride can be enhanced by as much as 7.6% through the integration of a single layer of graphene. In addition, The effect of the length, input power, and practical problems that may arise are studied on this structure in the presence and absence of an extra silicon-oxide/silicon substrate layer. The results show a great improvement in the nonlinear performance of this waveguide.

Acknowledgements

I would like to express my deepest appreciation to my supervisor Prof. A. H. Majedi. This work was not possible without his unwavering support. I have been extremely lucky to have a supervisor who cared so much about me and my work.

Dedication

I dedicate this work to my mother, who is strongly fighting with cancer. Her unconditional love and support inspires me to always do my best, and instills in me that I can do anything.

Table of Contents

List of Figures

ix

List of Tables

List of Symbols

σ Conductivity

ϵ_0 The free space permittivity

ϵ_r Relative permittivity

μ_0 The free space magnetic permeability

μ_r Relative permeability of material

χ Susceptibility

ω Angular frequency

μ_c The chemical energy potential of the band structure

λ Wavelength

Γ Phenomenalogical scattering rate

h Planck's constant

$\hbar$ Reduced Planck's constant

e The electron elementary charge

T	Temperature unit Kelvin
E_f	Fermi energy
v_f	The Fermi velocity
f_d	Fermi-Dirac distribution
k	The propagation constant
β	The real part of propagation constant
α	Loss
τ	Relaxation time
K_B	The Boltzmann Constant

Chapter 1

Introduction

The basis for all-optical signal generation and processing is formed by the third-order optical nonlinearity, which benefits from higher speed and bandwidth compared to electronic based devices [3, 4]. The third-order nonlinear response describes four wave mixing (FWM) has many applications in optical frequency comb generation [5, 6], optical sampling [7, 8], wavelength conversion [9, 10], sampling [7, 8] quantum entanglement [11, 12], and ultra fast optical oscilloscope [13].

By implementing nonlinear photonic devices in the form of integrated photonic devices, we may design a compact sized device, which offers higher stability, and scalability [14, 15, 16].

1.1 Research motivation

The leading platform for integrated photonic devices is silicon for many reasons. One of the main reasons is that this material is compatible with metal-oxide-semiconductor (CMOS) fabrication method [17, 14]. Although, one of the main limitations of silicon is the strong two photon absorption (TPA) of this material in the near-infrared wavelengths, which is a fundamental limitation for using it in the telecommunication wavelengths [18]. To address this problem, other CMOS compatible materials with low TPA such as silicon-nitride are suggested, but silicon-nitride suffers from the low intrinsic Kerr nonlinear response [19, 15]. In order to enhance the third-order nonlinear response of silicon-nitride, this paper suggests adding a layer of graphene to silicon-nitride.

Graphene has recently gained a lot of attention due to its unique optical properties, in particular, its exceptional high Kerr nonlinear response, which corresponds to the high optical susceptibility of this material [20, 21]. This two-dimensional material is also compatible with CMOS fabrication technology, making it a great candidate to augment the Kerr nonlinear optical response of silicon-nitride waveguide [22, 2]. This graphene integrated waveguide not only can be used in different applications such as spatial optical Solitons and squeezed quantum states [23, 24], but can also function as an electro-optical modulator if DC voltage is applied to the graphene layer [25].

1.2 Thesis objectives and contribution

This thesis reports a simulation, analysis, and design of graphene assisted silicon-nitride waveguide. The finite difference time domain (FDTD) simulation method is used to study the effect of adding a single layer of graphene to silicon-nitride on the nonlinear optical response, and the results are compared with those of the commercial software Lumerical FDTD. A detailed length and power analysis are performed on this waveguide, and the results are compared with theoretical analysis. The practical issues that may occur due to fabrication are discussed and addressed.

1.3 Outlines

This thesis presents the simulation, analysis, and design of graphene integrated silicon-nitride waveguide. The nonlinear performance of this waveguide has been investigated, including length and input power analysis.

Chapter 2 describes the linear and nonlinear optical properties of graphene. In chapter 3, we present the simulation methodology of graphene, and we investigate the behavior of a dielectric optical waveguide which is partially integrated with a single layer of graphene in order to study the effect of adding a single layer of graphene on a dielectric waveguide.

In chapter 4, we present the behavior of graphene integrated silicon-nitride waveguide, and compare it with theoretical results. In addition, we simulate a feasible graphene integrated silicon-nitride waveguide in the presence of an extra silicon-oxide/silicon substrate layer.

Chapter 2

Optical properties of graphene

This chapter presents the linear and nonlinear optical properties of graphene. As graphene is a two-dimensional material [26], unlike bulk materials the linear and nonlinear behavior of it is expressed using linear and nonlinear conductivity[2]. The energy band diagram of the graphene is shown in Figure 2.1 [27].

The intraband transition is a quantum mechanical process between levels within a conduction or valence band, which the optical nonlinearity is contributed by these transitions [28]. In case of having a transition between two different bands, the transition is called interband[29], which is more typical electron-hole interactions between conduction and valence bands [30, 31].

Both of these transitions are responsible for the conductivity, and the amount of their contribution depends on the frequency ω and chemical potential μ. The total two-dimensional conductivity can be expressed as below [32, 33]:

$$\sigma = \sigma_{intra} + \sigma_{inter} = \sigma' + i\sigma'' \tag{2.1}$$
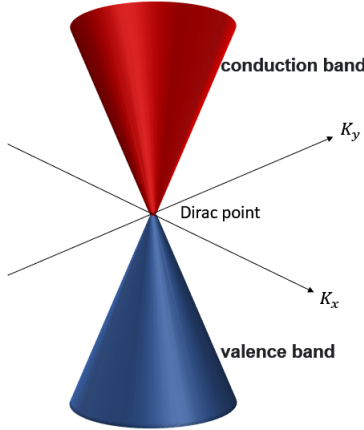
Figure 2.1: The energy band diagram of Graphene. The conduction band and valence band are shown in blue and red respectively. Unlike most materials, there is no band-gap between valence and conductive band of graphene, but there are different ways to open up a gap in the graphene band diagram such as strong circularly polarized light[1]. The point which conduction band and valence band meet is called Dirac point.

2.1   Linear optical properties of graphene

The induced polarization by an external electric field to a material can be characterized by electric susceptibility or so called optical susceptibility. The general form of susceptibility is a second-order tensor expressed as a function of x,y, and z which are spatial variables, because electric field and polarization are vectors [34]:

$$\chi(x,y,z) = \begin{bmatrix} \chi_{xx}(x,y,z) & \chi_{xy}(x,y,z) & \chi_{xz}(x,y,z) \\ \chi_{yx}(x,y,z) & \chi_{yy}(x,y,z) & \chi_{yz}(x,y,z) \\ \chi_{zx}(x,y,z) & \chi_{zy}(x,y,z) & \chi_{zz}(x,y,z) \end{bmatrix}. \tag{2.2}$$

Assuming the applied electric field is either parallel or perpendicular to the graphene sheet, the the direction of induced polarization will be same as the direction of applied electric field due to the symmetric structure of graphene. In addition, assuming the thickness of graphene is d $(-d/2 < z < d/2)$ the equation (2.2) reduces to [35]:

$$\chi(x, y) = \begin{bmatrix} \chi_x(x,y) & 0 & 0 \\ 0 & \chi_y(x,y) & 0 \\ 0 & 0 & \chi_z(x,y) \end{bmatrix}. \tag{2.3}$$

However, as graphene is not an isotropic material due to its hexagonal lattice structure, the linear optical properties of graphene is isotropic in x and y principal axes direction (where the surface of graphene is located)[2]. As a result, one can write:

$$\chi_x(x,y) = \chi_y(x,y) = \chi_\|(x,y)$$
$$\chi_z(x,y) = \chi_\perp(x,y), \tag{2.4}$$

finally, the susceptibility of graphene with in the limit of $-d/2 < z < d/2$ can be written as:

$$\chi(x, y) = \begin{bmatrix} \chi_\|(x,y) & 0 & 0 \\ 0 & \chi_\|(x,y) & 0 \\ 0 & 0 & \chi_\perp(x,y) \end{bmatrix}. \tag{2.5}$$

In the frequency domain, The relationship between polarization, susceptibility, and the applied electric field is:

$$p_x(x,y) = \epsilon_0 \chi_\|(x,y) E_x(x,y)$$
$$p_y(x,y) = \epsilon_0 \chi_\|(x,y) E_y(x,y) \tag{2.6}$$
$$p_z(x,y) = \epsilon_0 \chi_\perp(x,y) E_z(x,y),$$

where p is the polarization, and ϵ_0 is the vacuum permittivity. Now, the total permittivity can be obtained as[36]:

$$\epsilon(\omega) = \epsilon_0[1 + \chi(\omega)] + i\frac{\sigma(\omega)}{\omega}. \tag{2.7}$$

So far we have modeled the three-dimensional polarization, susceptibility, and permittivity assuming they are homogeneous in the z direction. The corresponding two-dimensional polarization, susceptibility, and permittivity can be written as[37]:

$$\tilde{\chi} = \chi d$$
$$\tilde{p} = pd \quad\quad\quad (2.8)$$
$$\tilde{\epsilon} = \epsilon d$$

The permittivity also is a tensor, which has the form of:

$$\epsilon = \begin{bmatrix} \epsilon_\parallel & 0 & 0 \\ 0 & \epsilon_\parallel & 0 \\ 0 & 0 & \epsilon_\perp \end{bmatrix}, \quad\quad\quad (2.9)$$

where $\epsilon_\parallel = \epsilon_0[1 + \tilde{\chi}_\parallel/d] + i\frac{\tilde{\sigma}_\parallel}{\omega d}$, and $\epsilon_\perp = \epsilon_0[1 + \tilde{\chi}_\perp/d]$. It should be noted that $\tilde{\sigma}_\perp$ is zero because free electrons of graphene are able to move only on the surface of the graphene.

2.1.1 Linear conductivity of graphene

When we introduce a layer of Graphene on the top of the waveguide, optical dispersion and absorption occurs due to Graphene coupling with the waveguide mode, which can be modeled by a complex dynamic conductivity. The linear conductivity of graphene can be expressed as sum of two terms respectively based on interband and intraband transitions [2, 38]:

$$\sigma(\omega, \Gamma, \mu_c, T) = \sigma_{intra}(\omega, \Gamma, \mu_c, T) + \sigma_{inter}(\omega, \Gamma, \mu_c, T),$$
$$\sigma_{intra}(\omega, \Gamma, \mu_c, T) = \frac{ie^2}{\pi\hbar^2(\omega - i2\Gamma)} \int_0^\infty \epsilon\left(\frac{\partial f_d(\epsilon)}{\partial \epsilon} - \frac{\partial f_d(\epsilon)}{\partial \epsilon}\right)d\epsilon, \quad\quad (2.10)$$
$$\sigma_{inter}(\omega, \Gamma, \mu_c, T) = \frac{-ie^2(\omega - i2\Gamma)}{\pi\hbar^2} \int_0^\infty \frac{f_d(-\epsilon) - f_d(\epsilon)}{(\omega - i2\Gamma)^2 - 4(\frac{\epsilon}{\hbar})^2}d\epsilon,$$

where ω is angular frequency of the source, ϵ is energy, e is electron charge, $\hbar$ is reduced plank's constant, T is temperature, Γ and μ_c are phenomenalogical scattering rate, chemical potential of graphene respectively, and $f_d(\epsilon) = \frac{1}{exp(\frac{\epsilon - \mu_c}{k_B T} + 1)}$ is the Fermi-Dirac distribution.

At room temperature under the condition of $\hbar\omega < 2\mu_c$, the intraband part of conductivity is negligible, but if we increase the frequency such that $\hbar\omega \approx 2\mu_c$, it becomes the

dominant term[39, 38]. If $k_B T << \mu_c$, the interband part of linear conductivity can be approximated as [38, 40]:

$$\sigma_{intra}(\omega, \Gamma, \mu_c, T) = \frac{-ie^2 k_B T}{\pi \hbar^2 (\omega - i2\Gamma)} [\frac{\mu_c}{k_B T} + 2\ln(e^{-\frac{\mu_c}{k_B T}} + 1)]. \qquad (2.11)$$

The conductivities are written with the assumption that the time harmonic form is $e^{i\omega t}$. If we consider the time harmonic as $e^{-i\omega t}$ the sign of the i in conductivity equations has to be changed. This simulation has been done assuming the temperature $T = 300\ K$, and the phenomenalogical scattering rate of graphene $\Gamma = 0.43\ ev$.

2.2 Nonlinear Optical properties of graphene

As graphene is a centro-symmetric two-dimensional material, which is made of hexagonal carbon lattice [22], the even harmonics do not form in this material [41]. once graphene gets irradiated by a harmonic electromagnetic wave with the frequency of ω it will generate higher odd harmonics $3\omega, 5\omega, ...$, which can vary from microwave to infrared [25].

The nonlinear optical behavior of materials can be described by the polarization, shown in equation (2.12) [41]:

$$P(t) = \epsilon_0 [\chi^{(1)} E(t) + \chi^{(2)} E^2(t) + \chi^{(3)} E^3(t) + ...] = P^{(1)} + P^{(2)} + P^{(3)} + ..., \qquad (2.12)$$

where $\chi^{(n)}$ is the nth order susceptibility, and $P^{(n)}$ is the nth order nonlinear polarization. It should be noted that we have assumed that the susceptibilities local responses are just function of time but not space, so equation (2.12) should be written in another form. For instance, the first order polarization will be equal to the convolution between susceptibility and electric field as shown in equation (2.13)[2]:

$$P^{(2)}(\vec{r}, t) = \epsilon_0 \int_{-\infty}^{t} \chi^{(1)}(t - \tau) . E(r, \tau) d\tau, \qquad (2.13)$$

where $\vec{r}$ is position vector. In this work, graphene is modeled as a current sheet because it is a two dimensional material and can be considered as a conductor. In order to do this

modeling, we assume a layer of graphene sheet located at $z = 0$ plane, which is illuminated by a monochromatic plane wave in $\hat{x}$ direction shown in equation (2.14).

$$E(r,t) = E_x(e^{ikz-i\omega t} + e^{-ikz+i\omega t})\hat{x}, \tag{2.14}$$

where E_x is the amplitude of the field and ω is the angular frequency of the incident beam. Assuming the graphene layer is located at $z = 0$ plane, equation (2.14) reduces to equation (2.15).

$$E(t) = E(x,y,0,t) = E_x(e^{-i\omega t} + e^{+i\omega t}) = 2E_x cos(\omega t). \tag{2.15}$$

The energy experienced by the electrons of the graphene sheet because of the applied electric field is $eE(t)$ where e is the electron charge $1.6 \times 10^{-19}C$. The momentum produced by this energy is $\hbar k$ where $\hbar$ is reduced plank's constant $\hbar = \frac{h}{2\pi} = 6.5 \times 10^{-16}eVs$.

$$\hbar\frac{dk_x}{dt} = -2eE_x cos(\omega t) \rightarrow \hbar k_x = \frac{-2eE_x sin(\omega t)}{\omega}, \tag{2.16}$$

The carrier velocity of graphene could be derived by Boltzmann transport equation, which gives the exact response of the system, which is independent from the amplitude of incident electric field [22]. Using this approach, we just consider the intraband contribution to the electric current. It should be noted that the interband transitions also have a contribution in this current, due to transitions between hole and electron bands, but as it is so small we have not considered the interband transition of graphene [25].

$$v_x = v_f\frac{k_x}{|k|} \rightarrow v_x = -v_f sgn(sin\omega t). \tag{2.17}$$

The surface current density of graphene obtained from the carrier velocity can be written as:

$$J_x(t) = -e\tilde{n}v_x = e\tilde{n}v_f sgn(sin\omega t) = e\tilde{n}v_f\frac{4}{\pi}(sin\omega t + \frac{1}{3}sin3\omega t + \frac{1}{5}sin5\omega t + ...). \tag{2.18}$$

As graphene is a two-dimensional material, the electron density of it should be two-dimensional, and it is shown by $\tilde{n}$. As we expected, equation (2.18) contains all odd harmonics, which arises from the centrom-symmetric structure of graphene's crystal. Owing to the linear band structure of graphene, the high order harmonics are appeared in

equation (2.18). The carrier velocity will be proportional to the applied electric field for materials with parabolic band structure, and as a result, the current will contain only one component of angular frequency.

The amplitude of harmonics decreases slowly $(\frac{1}{3}, \frac{1}{5}, ...)$ as the harmonic number increases. It is worth mentioning that we have not considered the Fermi distribution of charge carriers over the quantum states in the conduction and valence bands.

Starting from Boltzmann equation of motion, shown in equation (2.19):

$$\frac{\partial f}{\partial t} + F.\nabla_p f + v.\nabla_r f = (\frac{\partial f}{\partial t})_{coll}, \tag{2.19}$$

where f is the distribution function, which gives the probability of an electron having a specific momentum, position, and time. F is an external force, caused by the incident electric field, and v is the velocity of the electron. It should be noted that the phrase $(\frac{\partial f}{\partial t})_{coll}$ shows the changing rate of f in respect to scattering events.

Using relaxation time approximation, the right hand side of equation (2.19) becomes [2, 42]:

$$(\frac{\partial f}{\partial t})_{coll} = -\frac{f - f_0}{\tau}, \tag{2.20}$$

where f_0 is thermal equilibrium Fermi-Dirac distribution, and τ is relaxation time constant. Assuming the relaxation time as zero $\tau^{-1} = 0$ (i.e. no scattering effect), and knowing the applied force to the electrons of graphene is $F = -eE$, equation (2.19) can be written as:

$$\frac{\partial f_p}{\partial t} + \frac{\partial f_p}{\partial p_x} e E_0 e^{\alpha t} cos(\omega t) = 0. \tag{2.21}$$

The equation (2.21) can be solved using the characteristics method. In the absence of an external electric field, the distribution function of graphene becomes thermal equilibrium Fermi–Dirac distribution shown in equation (2.22):

$$f_0(p_x, p_y) = \frac{1}{exp[(v_f\sqrt{p_x^2 + p_y^2} - \mu)/k_B T] + 1}. \tag{2.22}$$

As the distribution function is constant along each characteristic curve of $k_x = \frac{-2eE_x cos(\omega t)}{\hbar}$, the solution of equation (2.21) in presence of external electric field will be:

$$f(k, t) = f_0(p_x + \frac{2eE_x}{\omega} sin\omega t, k_y). \tag{2.23}$$

In the limit, which the applied electric field satisfies the condition of $df/dE \approx df_0/dE$ the electric current density induced in graphene is [2] :

$$J = J_e + J_h = -e\frac{g}{(2\pi)^2} \int \int v_x f dk + e\frac{g}{(2\pi)^2} \int \int v_x(1-f)dk, \tag{2.24}$$

where j_e and j_h are electron and hole current, respectively. For graphene we assume $g = 4$, which is responsible for valley and spin degeneracies, and $v_x = v_f k_x/k$ is the velocity in the x direction because our assumed electric field is x-polarized [22, 2].

If the electric field satisfies the condition of $E_F >> k_B T$, the hole current can be ignored and $\mu = E_f$[2]. In this condition, the real surface current of graphene induced by the x-polarized electric field can be obtained using equation (2.24) and 2.23.

$$J_x(t) + J_x^*(t) = \frac{-ev_f}{\pi^2} \int_0^{2\pi} \int_0^\infty cos(\theta)f_0(kcos(\theta) + \frac{2eE_x}{\hbar\omega}sin(\omega t), ksin(\theta))kdkd\theta. \tag{2.25}$$

The relation between the complex vector current of graphene $(\boldsymbol{J}(t))$ and the complex current scalar $(J_x(t))$ is $\boldsymbol{J}(t) = \hat{x}J_x(t)$. Assuming the electric field is weak, equation (2.25) can be approximated as:

$$J_x(t) + J_x^*(t) \approx 2e\tilde{n}v_f\tilde{E}_x[(1 - \frac{3}{8}\tilde{E}_x)sin(\omega t) + \frac{1}{8}\tilde{E}_x^2 sin(3\omega t)], \tag{2.26}$$

where $\tilde{E}_x$ is so called dimensionless field strength parameter, which is the ratio of the energy experienced by the electrons of graphene during one oscillation to the Fermi energy of that electron.

$$\tilde{E}_x = \frac{ev_f}{\omega E_f}E_x. \tag{2.27}$$
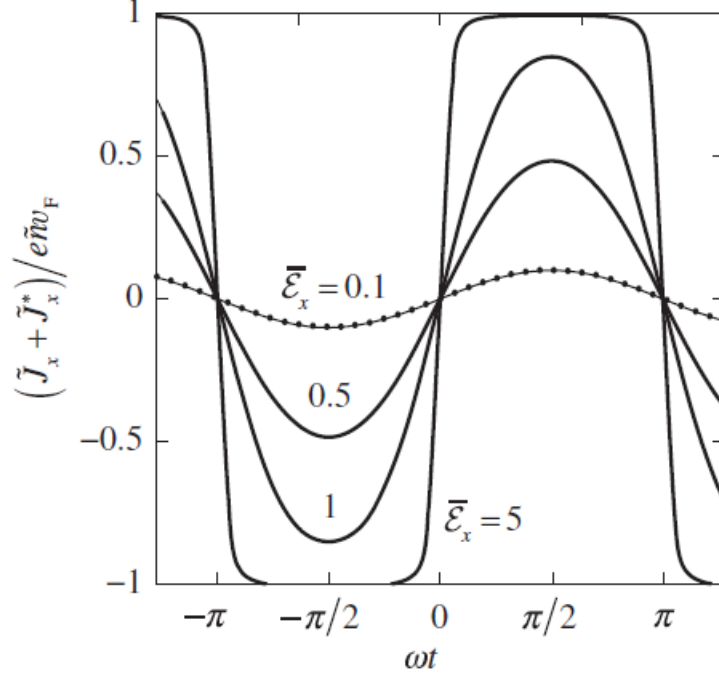
Figure 2.2: Surface current response of graphene, plotted using equation (2.25) for different field strengths. The $\tilde{E}_x$ is shown next to each curve, and the weak field approximation (equation (2.26)) is shown by dot symbol for $\tilde{E}_x = 0.1$. [2]

In the limit of $\tilde{E}_x << 1$, the equation (2.26) is a great approximation of the induced current. Having a strong external electric field $\tilde{E}_x << 1$, as the provided energy by the external electric field is higher than the Fermi energy, the carrier distribution is determined more by the applied electric field. Having this in mind, one can consider only the kinetic response of electrons to the applied electric field. In this case equation (2.18) best describes the behavior of graphene.

Equation (2.28) describes the relation between surface current density of graphene and the applied field.

$$
\begin{aligned}
J_x = \sigma_{xx}^{(1)}(\omega = \omega)(E_x e^{-i\omega t}) + \sigma_{xxxx}^{(3)}(\omega = \omega + \omega - \omega)(E_x e^{-i\omega t})^2 (E_x e^{i\omega t}) \\
+ \sigma_{xxxx}^{(3)}(3\omega = \omega + \omega + \omega)(E_x e^{-i\omega t})^3.
\end{aligned}
\tag{2.28}
$$

Comparing equation (2.26) with equation (2.28) the Drude intraband conductivity of graphene with the limitation of $E_f >> k_B T$ and $\frac{1}{\tau} \approx 0$ can be obtained[2].

$$\sigma_{xx}^{(1)} = \frac{ie^2 E_f}{\pi \hbar^2 \omega},$$

$$\sigma_{xxxx}^{(3)}(\omega = \omega + \omega - \omega) = \frac{-i3e^4 v_f^2}{8\pi \hbar^2 \omega^3 E_f}, \qquad (2.29)$$

$$\sigma_{xxxx}^{(3)}(3\omega = \omega + \omega + \omega) = \frac{ie^4 v_f^2}{8\pi \hbar^2 \omega^3 E_f}.$$

2.2.1 Experimental results

Many experiments have been done on nonlinear optical properties of graphene, and in almost all of them high values of Kerr nonlinear response has been reported. Some examples of these works are mentioned in table 2.1. The main methods of measuring the third-order nonlinearity of graphene are Z-scan, pump-probe, and four wave mixing.

Paper	Method	Result
[43]	Z-scan	NLO response of graphene observed
[44]	Z-scan	third harmonic generation
[45]	Z-scan	third harmonic generation
[46]	pump-probe	calculation of n2
[47]	chirped-pulse-pumped SPM	Kerr nonlinearity
[48]	four-wave mixing	intensity increases as a function of graphene layers

Table 2.1: Experimental results of nonlinear response of graphene

Chapter 3

Graphene-based photonic waveguides

Studying the effect of adding a layer of graphene on a waveguide, we used the FDTD simulation method. First, the simulation method used to simulate graphene is explained, then a simple dielectric waveguide which is partially integrated with graphene is simulated using this method. It should be noted that the graphene is available in the material bank of lumerical, and this software uses a slightly different method from what we will explain for graphene simulation. But the results obtained from both methods strongly agree with each other.

3.1 Graphene FDTD modeling

As graphene is a two-dimensional material, we model it as a current sheet. The total current used to model graphene can be written as sum of linear and nonlinear current[26]:

$$\tilde{\boldsymbol{J}}(\omega) = \tilde{\boldsymbol{J}}_L(\omega) + \tilde{\boldsymbol{J}}_{NL}(\omega) = (\sigma + \sigma_3|E|^2)\tilde{\boldsymbol{E}}(\omega). \tag{3.1}$$

Equation (3.1) is in the frequency domain. In order to perform a time domain simulation of graphene, we need to transfer this equation into the time domain.

3.1.1 Modeling the linear behavior

Under conditions where intraband term is the dominate part, using equation (2.11) we can write the linear part of total current as [49]:

$$(i\omega + 2\Gamma)\tilde{\boldsymbol{J}}_{\boldsymbol{L}}(\omega) = (\frac{e^2 k_B T}{\pi\hbar^2}A) \times \tilde{\boldsymbol{E}}(\omega), \tag{3.2}$$

where $A = \frac{\mu_c}{k_B T} + 2\ln(\exp(-\mu_c/k_B T) + 1)$. Using the Fourier transform property $\frac{\partial}{\partial t}x(t) \xrightarrow{\mathcal{F}} i\omega X(\omega)$, we are able to convert the frequency domain equation (3.2), to equation (3.3) ,which is in the time domain [50].

$$\frac{\partial}{\partial t}\boldsymbol{J}_L(t) + 2\Gamma\boldsymbol{J}_L(t) = (\frac{e^2 k_B T}{\pi\hbar^2} \times A) \times \boldsymbol{E}(t). \tag{3.3}$$

Equation (3.3) can be used as a time domain model for linear behavior of graphene, and it can implemented by finite difference time domain analysis as:

$$(\frac{J^{n+\frac{3}{2}} - J^{n+\frac{1}{2}}}{\Delta t}) + \Gamma(J^{n+\frac{3}{2}} + J^{n+\frac{1}{2}}) = (\frac{e^2 k_B T}{\pi\hbar^2}A) \times E^{n+1}. \tag{3.4}$$

3.1.2 Modeling the nonlinear behavior

As gephene can be considered as a conductor, we may model its nonlinear properties by a current which is a nonlinear function of incident electric field. In section 2.2 The nonlinear conductivity is discussed and generally it can be expressed as [51]:

$$\sigma_3(\omega) = \frac{i3e^4 v_f^2}{32\pi\hbar^2\mu\omega^3}. \tag{3.5}$$

For analyzing the nonlinear behavior of graphene, the nonlinear current obtained from nonlinear conductivity is used. Applying the same Fourier transform in equation (3.5), we can do the conversion from the frequency domain to the time domain as shown in equation (3.6).

$$\frac{\partial^3}{\partial t^3}\boldsymbol{J}_{NL}(t) = \frac{3}{32}\frac{e^2}{\pi\hbar^2}\frac{(ev_f)^2}{\mu}|E|^2\boldsymbol{E}(t). \tag{3.6}$$

As equation (3.6) is in the time domain, we are able to implement it in FDTD simulation, as shown in equation (3.7) [52].

14

$$\frac{J^{n+\frac{3}{2}} - 3J^{n+\frac{1}{2}} + 3J^{n-\frac{1}{2}} - J^{n-\frac{3}{2}}}{\Delta t^3} = \frac{3}{32} \frac{e^2}{\pi \hbar^2} \frac{(ev_f)^2}{\mu} E^3|_{i,j}^{n+1}. \tag{3.7}$$

It should be noted, there are other methods for performing the FDTD simulation of graphene, such as using polarization [37, 53].

3.2 Graphene integrated dielectric waveguide

In order to study the effect of adding graphene on a waveguide, we add a single layer of graphene on the middle part of a dielectric waveguide. Figure 3.1 shows a simple dielectric waveguide with no top or lower cladding, which is partially integrated with a single layer of graphene. The dimensions of this waveguide are chosen such that it only supports TE_0 and TM_0 mode, and such that adding the graphene layer will not make the waveguide multi-mode. A detailed analysis of dielectric optical waveguide is provided in appendix A.
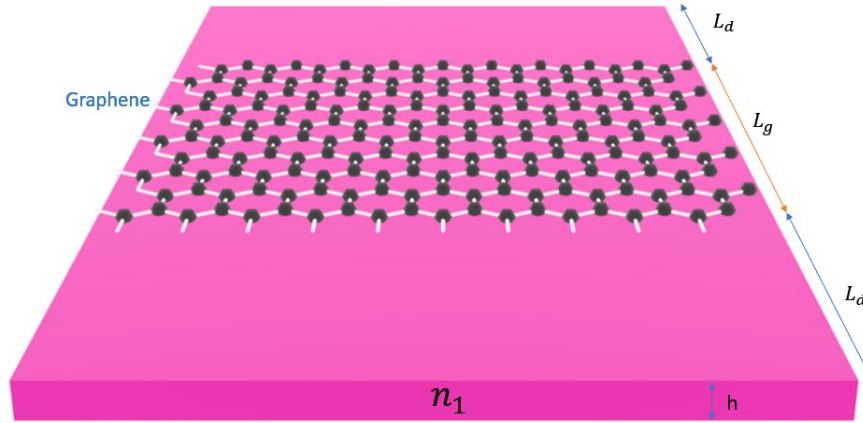
Figure 3.1: Dielectric waveguide which is partially integrated with graphene. The refractive index of the core is $n_1 = 1.3$, and the dimensions are $h = 200nm$ $L_d = L_g = 10\mu m$.

The source which is used to simulate graphene integrated dielectric waveguide is a single-frequency sinusoidal source with the wavelength of 1.55 μm, and the simulation has

been done considering TE modes. The relative permeability of the bulk materials is $\mu_r = 1$. Figure 3.2 shows the two-dimensional propagation of the electric field inside the waveguide. As the refractive index of graphene is higher than the core, the parts which are integrated with graphene have a higher effective refractive index. This higher refractive index leads to better wave confinement, and it is the reason for better confinement seen in Figure 3.2.
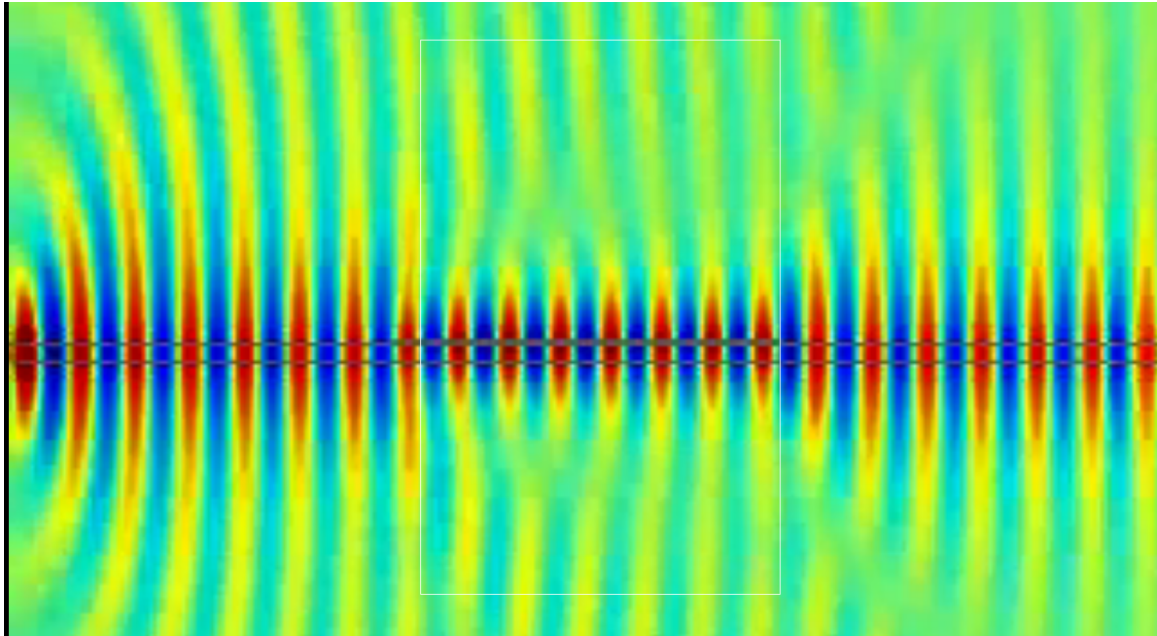
Figure 3.2: Two-dimensional electric field propagation inside the waveguide. The white square indicates the parts integrated with graphene. The better confinement seen in the white square is due to the higher effective refractive index of this region
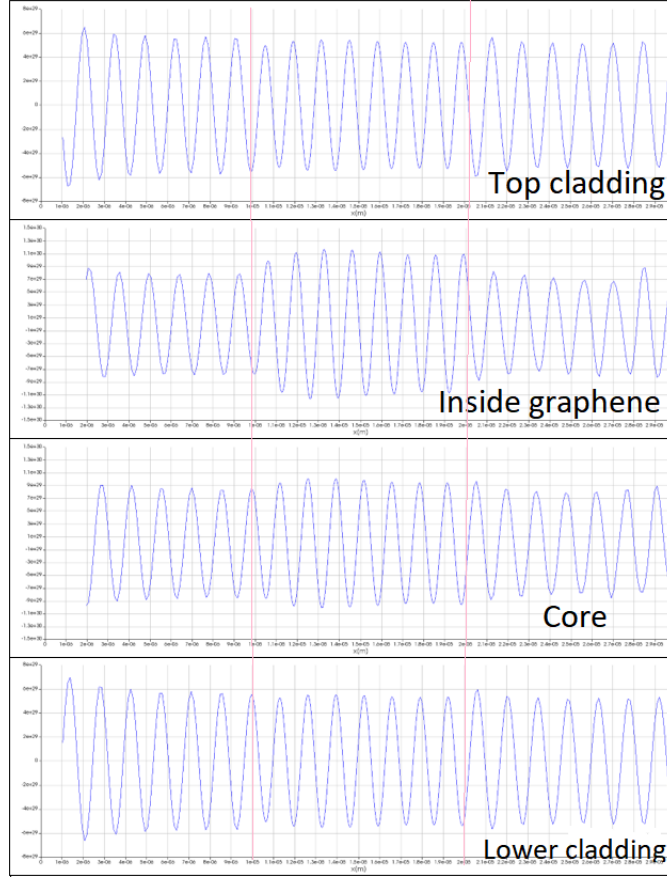
Figure 3.3: Electric field inside the core, graphene layer, top cladding, and lower cladding of the waveguide. The red lines indicate the parts integrated with graphene.

Figure 3.3 shows the electric field inside the different layers of the waveguide. Checking the electric field propagation in the core, an increasing in the amplitude of electric field can be observed at the beginning point of graphene. The reason of this increasing, is the better confinement resulted from the higher effective refractive index of this area.

Assuming a wave inside the waveguide is just consisted of the first and third harmonics, one can write it as:

$$A_1 cos(\omega t) + A_3 cos(3\omega t), \tag{3.8}$$

where the amplitude of the first harmonic is A_1 and the amplitude of the third harmonic is A_3.

We may calculate the amplitude of the generated third-order nonlinearity by taking Fourier transform from the time domain electric field shown in Figure 3.3. What we expect here is the graphene layer produces the third harmonic of the input source inside the core of the waveguide.
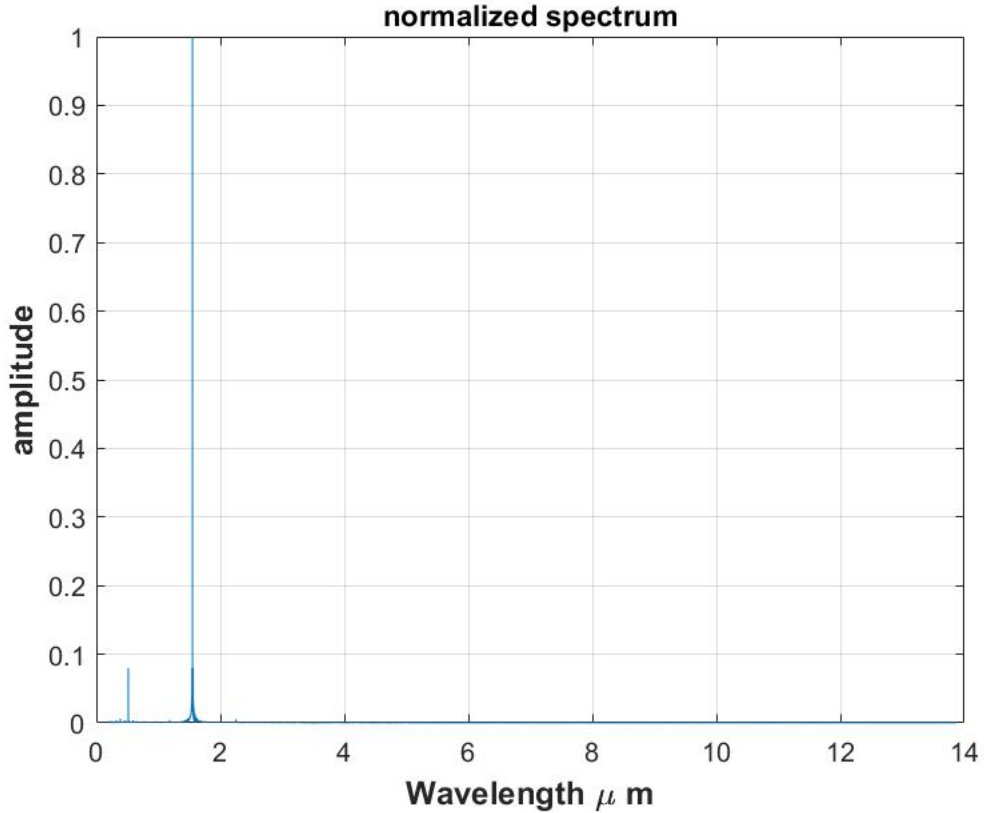
Figure 3.4: The spectrum of the the graphene integrated dielectric waveguide normalized to the amplitude of first harmonic generation. The second peak represents the third harmonic with the wavelength of $1.55m$, which is same as the wavelength of the source. The first peak represents the third harmonic generated by the graphene layer with the wavelength of $0.516\mu m$ and amplitude of 0.08 .

Figure 3.4, shows the spectrum of the waveguide. The third-order nonlinearity is generated due to the high Kerr nonlinear response of graphene. As expected, the amplitude of the third-order nonlinear response in the graphene layer is higher than the core layer.

It should be noted that, if using using the described FDTD method one should consider the beginning point of graphene at a distance from the source where the mode of the waveguide is formed. Otherwise the convergence of the code will be hard to achieve. But using Lumerical software, we can begin the graphene right after the source.

Chapter 4

Graphene integrated silicon-nitride waveguide

In this chapter, we design and investigate the behavior of graphene integrated silicon-nitride waveguide. First, we introduce the modeling method of silicon-nitride, then we compare the simulation results with the experimental results. In the next step, we represent the simulation flowchart, which can be used for the simulation of a structure consisted of multi linear and nonlinear layers. Then, we study the nonlinear behavior of graphene integrated silicon-nitride. In the last section, we perform a detailed simulation on a feasible waveguide structure, and we discuss and address the practical problems that may occur.

4.1   Modeling graphene integrated silicon-nitride

As Silicon-nitride is a bulk material, we do the simulation using the third-order susceptibility. In the Kerr-type nonlinear response, the relation between the refractive index n and the intensity of light I in the limit where $\chi^{(3)}|E(t)|^2 << \chi^{(1)}$ is given by [41]:

$$n = n_0 + n_2 I, \tag{4.1}$$

where the light intensity is $I = n_0 \sqrt{\frac{\epsilon_0}{\mu_0}} |E(t)|^2$. The n_2 of the silicon nitride of silicon nitride/silicon dioxide waveguides, which is our study case is $n_2 = 2.4 \times 10^{-15}$ cm^2/W [54]. The value of third-order susceptibility of silicon-nitride is calculated as $\chi^{(3)} = 5.095 \times 10^{-21} m^2/V^2$ using the following formula:

$$\chi^{(3)} = 2n_0^2 n_2 \sqrt{\frac{\epsilon_0}{\mu_0}}. \tag{4.2}$$

The nonlinear optical response of silicon-nitride can be described by polarization[41], and the electric flux density D can be written as:

$$\boldsymbol{D} = \epsilon_0 \epsilon_r \boldsymbol{E} + \boldsymbol{P}_{NL}, \tag{4.3}$$

where ϵ_0 is vacuum permittivity, ϵ_r is relative permittivity, and $\boldsymbol{P}_{NL}(t) = \epsilon_0 \chi^{(3)} \boldsymbol{E}^3(t)$ is the nonlinear polarization. Using the Maxwell's equation:

$$\nabla \times \boldsymbol{H} = \boldsymbol{J} + \frac{\partial \boldsymbol{D}}{\partial t}, \tag{4.4}$$

where H is the magnetic field , we can describe the graphene and silicon-nitride by current and electric flux density respectively.

Assuming TE propagation in the z direction, there will be three field components of E_y, H_x, and H_z in the waveguide. Assuming the waveguide is long enough in y direction that there is no variation in this direction ($\frac{\partial}{\partial y} = 0$), equation (4.4)becomes:

$$\nabla \times \boldsymbol{H} = \boldsymbol{J}_L(t) + \boldsymbol{J}_{NL}(t) + \epsilon_0 \epsilon_r \frac{\partial \boldsymbol{E}(t)}{\partial t} + 3\epsilon_0 \chi^{(3)} |E|^2 \frac{\partial \boldsymbol{E}(t)}{\partial t}, \tag{4.5}$$

where the $\boldsymbol{J}_{NL}(t)$ and $3\epsilon_0 \chi^{(3)} \boldsymbol{E}^2(t) \frac{\partial \boldsymbol{E}(t)}{\partial t}$ describe the nonlinear behavior of graphene and silicon-nitride respectively.

Figure 4.1 shows the flow chart used for the simulation of graphene integrated silicon-nitride waveguide.
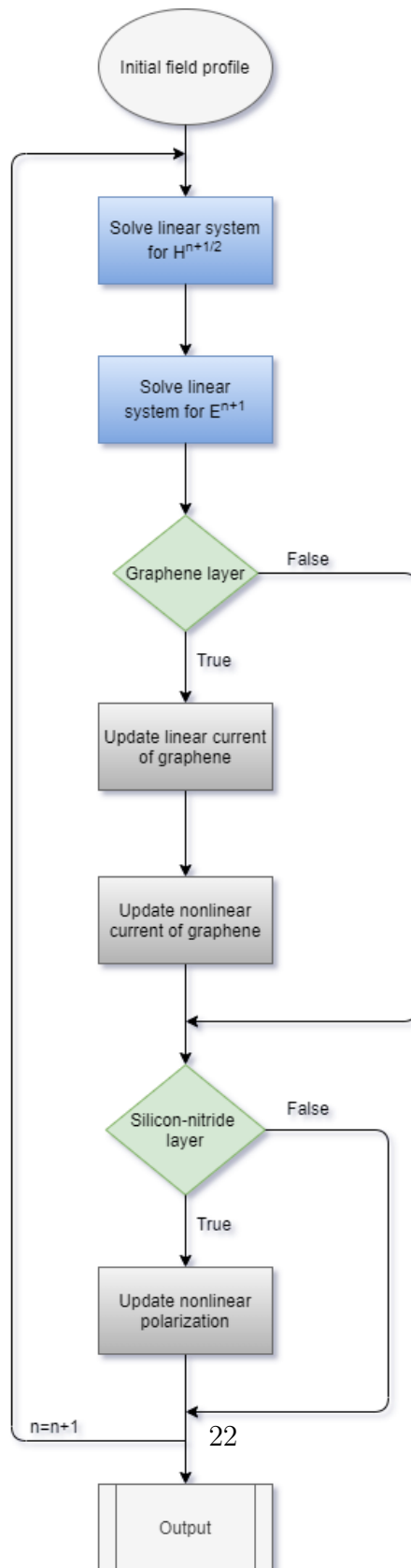
Figure 4.1: Flowchart of FDTD simulation of graphene integrated silicon-nitride waveguide.

4.2 Silicon-Nitride waveguide

Figure 4.2 shows the structure of a low loss single-stripe silicon nitride waveguide [55, 56]. Silicon-nitride waveguides not only is CMOS compatible [15], but also is broad transparency ranging from the visible to mid-infrared, including all the telecommunication bands [57].
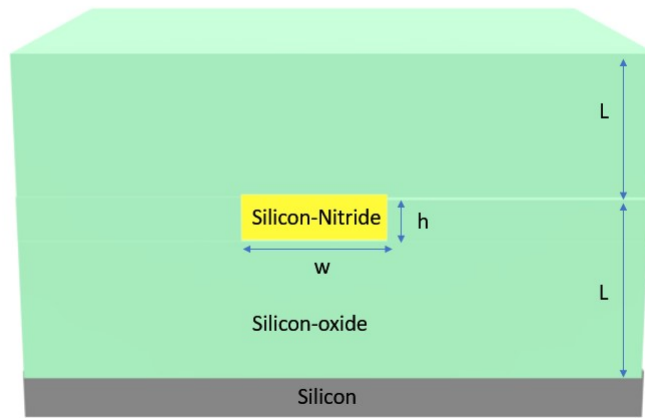
Figure 4.2: Single core silicon-nitride waveguide structure. The dimension of this waveguide is $w = 4.2~\mu m$, $h = 65~nm$, and $L = 15~\mu m$, and the thickness of silicon layer is $5~\mu m$.

The FDTD simulation on the waveguide structure shown in Figure 4.2 is performed considering TE modes and a single-frequency sinusoidal source with the wavelength of $1.55~\mu m$, and the waveguide parameters are calculated and compared with actual experimental results.

Figure 4.3 shows the two-dimensional electric field propagation inside the silicon-nitride waveguide. The guided wavelength obtained from the simulation is $\lambda_g = 1.06\mu m$, which the propagation constant can be calculated from using:

$$\beta = \frac{2\pi}{\lambda_g}. \tag{4.6}$$

Also, the effective refractive index can be calculated using the guided wavelength using:

$$n_{eff} = \frac{\beta}{k_0} = \frac{\lambda_0}{\lambda_g}, \tag{4.7}$$

where k_0 is the free space propagation constant.
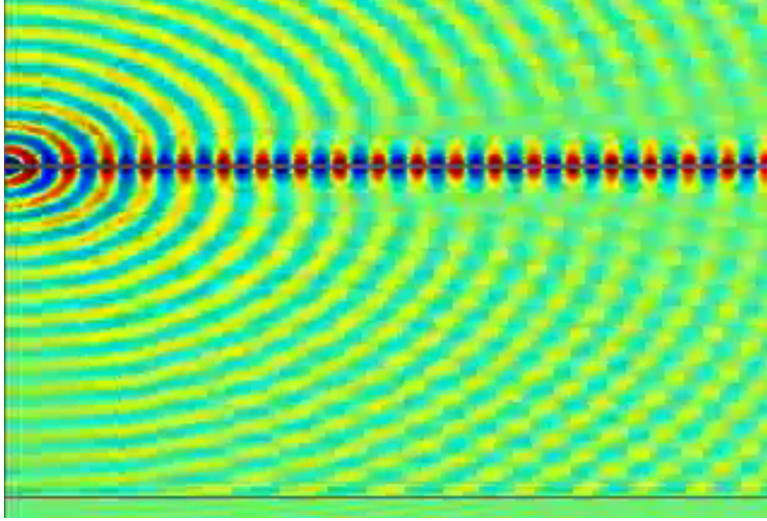
Figure 4.3: 2D propagation of electric field in SiN waveguide

The parameters obtained from the simulation of the silicon-nitride waveguide are compared with experimental results [55, 56] in table 4.1.

Parameter	Lumerical	Experimental Results
β	$5.927\mu m^{-1}$	$5.916\mu m^{-1}$
n_{eff}	1.462	1.459
$\alpha[dB/cm]$	0.028	≤ 0.03

Table 4.1: comparing waveguide Using simulation and Experimental results

All the parameters calculated using the FDTD simulation method, strongly agree with the experimental results. This shows that all the parameters we used to model different materials are describing the behavior of this structure perfectly.

24

4.3 Graphene integrated Silicon nitride

All the simulations have been done by the explained two-dimensional FDTD method, and the results have been compared with simulation results, obtained from the commercial software Lumerical FDTD. The results from both methods have been compared, and they strongly agree.
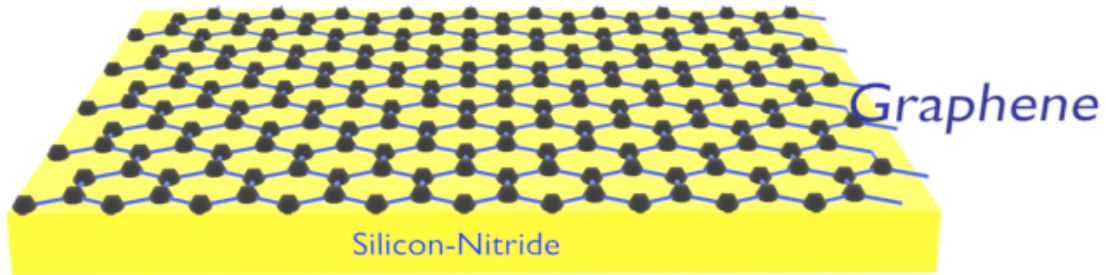
Figure 4.4: Silicon-Nitride waveguide with the thickness of 60 nm integrated with a single layer of graphene

First, we simulate the Silicon-Nitride waveguide shown in figure 4.4 without graphene. Then, we study the effect of adding a single layer of graphene to this structure.

It should be noted that, if using the described FDTD method one should consider the beginning point of graphene at a distance from the source where the mode of the waveguide is formed. Otherwise, the convergence of the code will be hard to achieve. But using Lumerical software, we can begin the graphene right after the source.

For this simulation we used a single single-frequency sinusoidal source with the wavelength of 1.55 μm, we have considered TE modes.
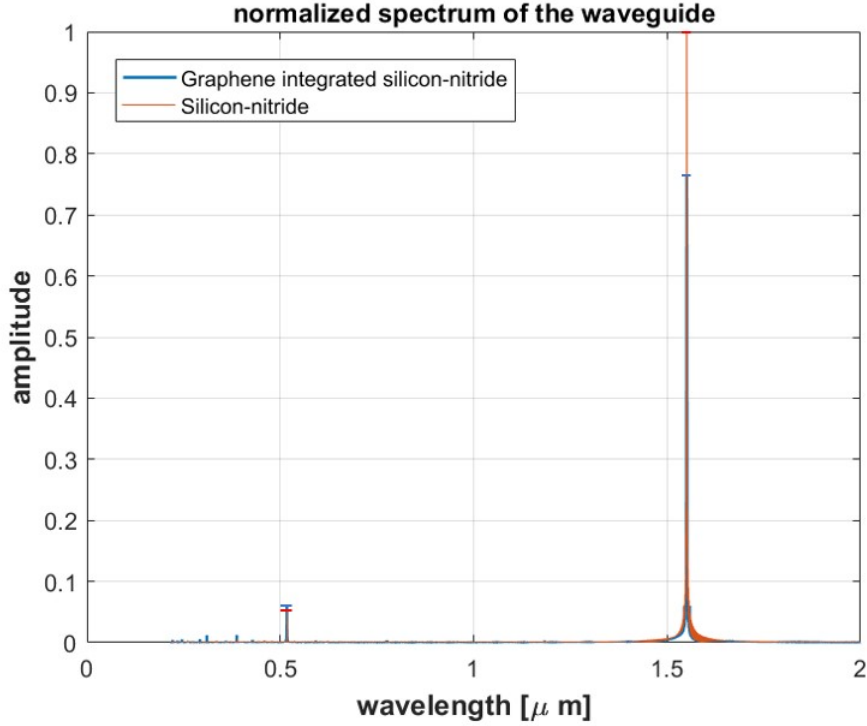
Figure 4.5: The spectrum at the center of the core of the silicon-nitride, and graphene integrated silicon-nitride waveguide normalized to the first harmonic amplitude of silicon-nitride waveguide. The second peak corresponds to the first harmonic respond of the waveguide with the wavelength of $1550nm$. The first peak corresponds to the third harmonic generation of the waveguide with the wavelength of $516.6nm$. By adding a single layer of graphene some the first order generation of the waveguide is decreased, and the third-order nonlinear response of the waveguide has been increased as much as 7.6%.

As shown in figure 4.5, by adding a single layer of graphene the third-order nonlinearity response of this structure is increased as much as 7.6%.

4.4   length analysis

In this section, we study the effect of the length of the graphene integrated silicon-nitride waveguide on the nonlinear response of it. First, we solve the coupled-amplitude

26

equations, which describes the third harmonic generation, assuming the material is loss-less, and considering processes described by susceptibility elements $\chi^{(3)}(3\omega; \omega, \omega, \omega)$, and $\chi^{(3)}(\omega; 3\omega, -\omega, -\omega)$, which are representing the conversion $3f \Rightarrow f$ and $f \Rightarrow 3f$, to calculate the intensity of the third harmonic wave as a function of length.

The total electric field in the nonlinear medium can be written as:

$$\tilde{E}(z,t) = \tilde{E}_1(z,t) + \tilde{E}_2(z,t), \tag{4.8}$$

where each component is written in terms of a complex amplitude $E_j(z)$, and the slowly varying amplitude $A_j(z)$, which is:

$$\tilde{E}_j(z,t) = E_j(z)e^{-i\omega_j t} + c.c, \tag{4.9}$$

where:

$$E_j(z) = A_j(z)e^{ik_j z} \tag{4.10}$$

where the propagation constant is $k_j = \frac{n_j \omega_j}{c}$, and the refractive index is $n_j = \sqrt{\epsilon^{(1)}(\omega_j)}$.

We assume that each frequency component of the electric field obeys the equation of:

$$\frac{\partial^2 \tilde{E}_j}{\partial z^2} - \frac{\epsilon^{(1)}(\omega_j)}{c^2}\frac{\partial^2 \tilde{E}_j}{\partial t^2} = \frac{1}{\epsilon_0 c^2}\frac{\partial^2 \tilde{P}_j}{\partial t^2}. \tag{4.11}$$

The nonlinear polarization can be expressed as :

$$\tilde{P}^{NL}(z,t) = \tilde{P}_1(z,t) + \tilde{P}_2(z,t), \tag{4.12}$$

where $\tilde{P}_j(z,t) = P_j(z)e^{-i\omega_j t} + c.c.$ and $j = 1$ represents the first harmonic and $j = 2$ represents the third harmonic equation.

We are analyzing the processes described by the two susceptibility elements. The first one is $\chi^{(3)}(3\omega; \omega, \omega, \omega)$ which corresponds to third harmonic generation. The second one is $\chi^{(3)}(\omega; 3\omega, -\omega, -\omega)$ which corresponds to difference-frequency generation, and it happens when the third harmonic radiation is strong enough to produce difference frequency generation. As the medium is lossless, due to permutation symmetry, the frequency arguments of the nonlinear susceptibility are able to be freely interchanged, we can write:

$$\chi^{(3)}(3\omega; \omega, \omega, \omega) = \chi^{(3)}(\omega; 3\omega, -\omega, -\omega) = \chi^{(3)}, \tag{4.13}$$

As a result, the amplitude of $P_{1,2}(z)$ will be:

$$P_1(z) = 3\epsilon_0\chi^{(3)}E_2E_1^*E_1^* = 3\epsilon_0\chi^{(3)}A_2A_1^*A_1^*e^{(k_2-2k_1)z}, \tag{4.14}$$

$$P_2(z) = \epsilon_0\chi^{(3)}E_1^3 = \epsilon_0\chi^{(3)}A_1^3e^{3ik_1z}. \tag{4.15}$$

If substitute equation (4.14) into equation (4.11), we can calculate the equation of the first harmonic.

$$\frac{\partial^2\tilde{E}_j}{\partial z^2} - \frac{\epsilon^{(1)}(\omega_j)}{c^2}\frac{\partial^2\tilde{E}_j}{\partial t^2} = \frac{1}{\epsilon_0 c^2}\frac{\partial^2\tilde{P}_j}{\partial t^2} \Rightarrow (\frac{\partial^2 A_1}{\partial z^2},$$

$$+2ik_1\frac{\partial A_1}{\partial z} - k_1^2A_1)e^{i(k_1z-\omega_1t)} + \frac{\epsilon^{(1)}(\omega_1)\omega_1^2A_1}{c^2}e^{i(k_1z-\omega_1t)}, \tag{4.16}$$

$$= \frac{-3\chi^{(3)}\omega_1^2A_2A_1^*A_1^*}{c^2}e^{(ik_2-2ik_1)z}e^{-i\omega_1t}.$$

Considering propagation constant $k_j = \frac{n_j\omega_j}{c}$, and the refractive index is $n_j = \sqrt{\epsilon^{(1)}(\omega_j)}$ equation (4.16) becomes:

$$\frac{\partial^2 A_1}{\partial z^2} + 2ik_1\frac{\partial A_1}{\partial z} = \frac{-3\chi^{(3)}\omega_1^2A_2A_1^*A_1^*}{c^2}e^{(ik_2-2ik_1)z}e^{-i\omega_1t}. \tag{4.17}$$

Assuming slowly varying amplitude approximation $|\frac{\partial^2 A_1}{\partial z^2}| << |2ik_1\frac{\partial A_1}{\partial z}|$ and phase matching condition $k_2 = 3k_1$ equation (4.17) reduces to:

$$\boxed{\frac{\partial A_1}{\partial z} = \frac{3i\chi^{(3)}\omega_1^2A_2A_1^*A_1^*}{2k_1c^2}.} \tag{4.18}$$

Now, we do the same procedure substituting equation (4.15) in to equation (4.11) to obtain the third harmonic term:

$$2ik_2\frac{\partial A_2}{\partial z}e^{-i(\omega_2t-k_2z)} = \frac{-\omega_2^2\chi^{(3)}A_1^3}{c^2}e^{-i(\omega_2t-3k_1z)}. \tag{4.19}$$

From phase matching condition $k_2 = 3k_1$, we may write equation (4.19) as:

28

$$\boxed{\frac{\partial A_2}{\partial z} = \frac{i\omega_2^2 \chi^{(3)} A_1^3}{2k_2 c^2}.} \tag{4.20}$$

In general case, we should solve the pair of coupled equations simultaneously. To do so, instead of working with the complex quantities, we work with the modulus and phase of each field's amplitudes. In addition, these amplitudes are expressed in dimensionless form. As a result, the complex, slowly varying field amplitudes are written as:

$$A_1 = \sqrt{\frac{I}{2n_1 \epsilon_0 c}} u_1 e^{i\phi_1}, \tag{4.21}$$

$$A_2 = \sqrt{\frac{I}{2n_2 \epsilon_0 c}} u_2 e^{i\phi_2}, \tag{4.22}$$

where $I = <\frac{|E|^2}{\eta}>_t$ is optical intensity . Substituting these values in to equation (4.18) we get:

$$\frac{\partial A_1}{\partial z} = \frac{3i\chi^{(3)}\omega_1^2 A_2 A_1^* A_1^*}{2k_1 c^2} \Rightarrow \sqrt{\frac{I}{2n_1 \epsilon_0 c}} (\frac{\partial u_1}{\partial z} + iu_1 \frac{\partial \phi_1}{\partial z}) e^{i\phi_1} =$$

$$\frac{3i\chi^{(3)}\omega_1^2 \sqrt{\frac{I}{2n_2 \epsilon_0 c}} u_2 e^{i\phi_2} \frac{I}{2n_1 \epsilon_0 c} u_1^2 e^{-2i\phi_1}}{2\frac{n_1 \omega_1}{c} c^2} \Rightarrow (\frac{\partial u_1}{\partial z} + iu_1 \frac{\partial \phi_1}{\partial z}) =$$

$$\frac{3iI\chi^{(3)}\omega_1 \sqrt{\frac{1}{n_1 n_2}} u_2 e^{i\phi_2} u_1^2 e^{-3i\phi_1}}{4\epsilon_0 c n_1} (\frac{\partial u_1}{\partial z} + iu_1 \frac{\partial \phi_1}{\partial z}) = \tag{4.23}$$

$$\frac{3iI\chi^{(3)}\omega_1 \sqrt{\frac{1}{n_1 n_2}} u_2 u_1^2}{4\epsilon_0 c n_1} (cos(3\phi_1 - \phi_2) - isin(3\phi_1 - \phi_2)) \Rightarrow$$

$$\theta = 3\phi_1 - \phi_2 \Rightarrow (\frac{\partial u_1}{\partial z} + iu_1 \frac{\partial \phi_1}{\partial z}) =$$

$$\frac{3iI\chi^{(3)}\omega_1 \sqrt{\frac{1}{n_1 n_2}} u_2 u_1^2}{4\epsilon_0 c n_1} (cos(\theta) - isin(\theta)).$$

Now we do the same procedure for A_2

29

$$\frac{\partial A_2}{\partial z} = \frac{i\omega_2^2 \chi^{(3)} A_1^3}{2k_2 c^2} \Rightarrow \sqrt{\frac{I}{2n_2\epsilon_0 c}}(\frac{\partial u_2}{\partial z} + iu_2\frac{\partial\phi_2}{\partial z})e^{i\phi_2} =$$

$$\frac{i\omega_2^2\chi^{(3)}(\sqrt{\frac{I}{2n_1\epsilon_0 c}}u_1 e^{i\phi_1})^3}{2\frac{n_2\omega_2}{c}c^2} \Rightarrow (\frac{\partial u_2}{\partial z} + iu_2\frac{\partial\phi_2}{\partial z}) =$$

$$\frac{i\omega_2\chi^{(3)}I\sqrt{\frac{n_2}{n_1}}u_1^3 e^{i(3\phi_1-\phi_2)}}{4n_2n_1\epsilon_0 c^2}(\frac{\partial u_2}{\partial z} + iu_2\frac{\partial\phi_2}{\partial z}) = \qquad (4.24)$$

$$\frac{i\omega_2\chi^{(3)}I\sqrt{\frac{n_2}{n_1}}u_1^3}{4n_2n_1\epsilon_0 c^2}(cos(3\phi_1-\phi_2) + isin(3\phi_1-\phi_2)) \Rightarrow$$

$$\omega_2 = 3\omega_1, \theta = 3\phi_1 - \phi_2 \Rightarrow (\frac{\partial u_2}{\partial z} + iu_2\frac{\partial\phi_2}{\partial z}) =$$

$$\frac{3i\omega_1\chi^{(3)}I\sqrt{\frac{n_2}{n_1}}u_1^3}{4n_2n_1\epsilon_0 c^2}(cos(\theta) + isin(\theta)).$$

Separating real and imaginary part of equation (4.23) and equation (4.24), and introducing $M = \frac{3I\omega_1\chi^{(3)}}{4n_1\sqrt{n_1 n_2}\epsilon_0 c^2}$ we get:

$$\frac{\partial u_1}{\partial z} = Mu_1^2 u_2 sin(\theta), \qquad (4.25)$$

$$\frac{\partial\phi_1}{\partial z} = Mu_1 u_2 cos(\theta), \qquad (4.26)$$

$$\frac{\partial u_2}{\partial z} = -Mu_1^3 sin(\theta), \qquad (4.27)$$

$$\frac{\partial\phi_2}{\partial z} = M\frac{u_1^3}{u_2}cos(\theta). \qquad (4.28)$$

It is worth mentioning that from phase matching condition we may derive $n_2 = n_1$, which is shown below:

$$k_2 = 3k_1 \Rightarrow \frac{n_2\omega_2}{c} = \frac{3n_1\omega_1}{c} \Rightarrow$$

$$\omega_2 = 3\omega_1 \Rightarrow \frac{n_2 3\omega_1}{c} = \frac{3n_1\omega_1}{c} \Rightarrow n_2 = n_1 = n, \tag{4.29}$$

then, M becomes: $M = \frac{3I\omega_1\chi^{(3)}}{4n^2\epsilon_0 c^2}$.

To solve equations 4.25 to 4.28, we use a similar way used for solving similar equations for the second harmonic in [41].

Combining equation (4.26) and equation (4.28) we get:

$$3\frac{\partial\phi_1}{\partial z} - \frac{\partial\phi_2}{\partial z} = \frac{\partial\theta}{\partial z} = 3Mu_1u_2cos(\theta) - M\frac{u_1^3}{u_2}cos(\theta). \tag{4.30}$$

Introducing new variable $\zeta = Mz$ equations 4.25,4.27 and 4.30 reduce to:

$$\frac{\partial u_1}{\partial \zeta} = u_1^2 u_2 sin(\theta), \tag{4.31}$$

$$\frac{\partial u_2}{\partial \zeta} = -u_1^3 sin(\theta), \tag{4.32}$$

$$\frac{\partial\theta}{\partial \zeta} = (3u_1u_2 - \frac{u_1^3}{u_2})cos(\theta). \tag{4.33}$$

By calculating the expression $\frac{\partial ln(u_1^3 u_2)}{\partial \zeta} = \frac{3u_1^2 u_2 \frac{\partial u_1}{\partial \zeta} + u_1^3 \frac{\partial u_2}{\partial \zeta}}{u_1^3 u_2}$, we may simplify equations 4.31 and 4.32 as:

$$\frac{\partial ln(u_1^3 u_2)}{\partial \zeta} = \frac{3u_1^2 u_2 u_1^2 u_2 sin(\theta)\partial\zeta - u_1^3 u_1^3 sin(\theta)}{u_1^3 u_2} = (3u_1u_2 - \frac{u_1^3}{u_2})sin(\theta). \tag{4.34}$$

Using above result, we may write equation (4.33) as:

$$\frac{\partial\theta}{\partial \zeta} = \frac{cos\theta}{sin\theta}\frac{\partial ln(u_1^3 u_2)}{\partial \zeta}. \tag{4.35}$$

31

If we multiply both sides of equation (4.35) to $\frac{sin\theta}{cos\theta}$ we get:

$$\frac{sin\theta}{cos\theta}\frac{\partial\theta}{\partial\zeta} = \frac{-1}{cos\theta}\frac{\partial cos\theta}{\partial\zeta} = \frac{\partial - ln(cos\theta)}{\partial\zeta} = \frac{\partial ln(u_1^3 u_2)}{\partial\zeta} \Rightarrow$$
$$\frac{\partial(ln(u_1^3 u_2) + ln(cos\theta))}{\partial\zeta} = \frac{\partial(ln(u_1^3 u_2 cos\theta))}{\partial\zeta} = 0. \quad (4.36)$$

From above equation we may conclude that $ln(u_1^3 u_2 cos\theta)$ is a constant value. We can call this constant value $ln(u_1^3 u_2 cos\theta) = \Gamma$. In this case, we may write $sin\theta$ and $cos\theta$ in terms of Γ:

$$cos\theta = \frac{\Gamma}{u_1^3 u_2},$$

$$sin\theta = \pm\sqrt{1 - cos^2\theta} = \pm\sqrt{1 - \frac{\Gamma^2}{u_1^6 u_2^2}}. \quad (4.37)$$

Assuming the initial condition as $u_2(0) = 0$ and $u_1(0) = const = u_i$ which gives $\Gamma = const = ln(u_1^3 u_2 cos\theta) = 0$. As a result, from above equations we get $cos\theta = 0$ and $sin\theta = \pm 1$. Now, we may write equation (4.31) and equation (4.32) as:

$$\frac{\partial u_1}{\partial\zeta} = \pm u_1^2 u_2, \quad (4.38)$$

$$\frac{\partial u_2}{\partial\zeta} = \mp u_1^3. \quad (4.39)$$

Using the fact that $u_1^2 + u_2^2 = 1$ equation (4.39) can be written as:

$$\frac{\partial u_2}{\partial\zeta} = \mp\sqrt{(1 - u_2^2)^3}. \quad (4.40)$$

Now, we try to solve equation (4.40):

$$\int \frac{\partial u_2}{\mp\sqrt{(1-u_2^2)^3}\partial\zeta} = \int \partial\zeta \Rightarrow$$

$$\frac{u_2}{\mp\sqrt{1-u_2^2}} = \zeta + c = Mz + c. \tag{4.41}$$

Considering initial condition that $u_2(0) = 0$ we can conclude that $c = 0$

$$\frac{u_2}{\mp\sqrt{1-u_2^2}} = Mz \Rightarrow (\frac{u_2}{Mz})^2 = 1 - u_2^2 \Rightarrow u_2 = \pm\frac{Mz}{\sqrt{1+M^2z^2}}. \tag{4.42}$$

As $u_2 > 0$ we have:

$$u_2 = \frac{Mz}{\sqrt{1+M^2z^2}}. \tag{4.43}$$

Now we may calculate the A_2 from equation (4.22):

$$A_2 = \sqrt{\frac{I}{2n_2\epsilon_0 c}}u_2 e^{i\phi_2} = \sqrt{\frac{I}{2n_2\epsilon_0 c}}\frac{Mz}{\sqrt{1+M^2z^2}}e^{i\phi_2}. \tag{4.44}$$

considering, $I = I_1 + I_2 = const$

$$I_2 = 2n_2\epsilon_0 c|A_2|^2 = 2n_2\epsilon_0 c \times \frac{I}{2n_2\epsilon_0 c}\frac{M^2z^2}{1+M^2z^2} = \frac{IM^2z^2}{1+M^2z^2}. \tag{4.45}$$

Finally, we may write equation (4.45) as a function of L, noting that $I = I_1(0)$

$$\boxed{I_2 = \frac{I_1(0)M^2z^2}{1+M^2z^2}} \tag{4.46}$$

$$\boxed{M = \frac{3I_1(0)\omega_1\chi^{(3)}}{4n^2\epsilon_0 c^2}}$$

where I_1, and I_2 are first and third harmonic intensity respectively, and z is the length. It should be noted that, equation (4.4) shows the proportionality of the length effect, and does not show the exact value as we have not considered the power conversion efficiency.

The simulation results obtained from FDTD simulation have been compared with theoretical analysis obtained from equation (4.4). Figure 4.6 shows that two graphs are consistent with each other, and the nonlinear amplitude response becomes almost constant in the limit where $M^2 z^2 >> 1$. The values obtained from FDTD simulation are slightly smaller than the theory results, because in the theory we have not considered that amount of the wave, that leaves the waveguide. Figure 4.6 shows that in this structure, the Kerr nonlinear response increases dramatically with in the length limit of 0 μm to 5 μm, and when the length gets longer than 15 μm the Kerr nonlinearity does not change much within the limit of $M^2 z^2 >> 1$.
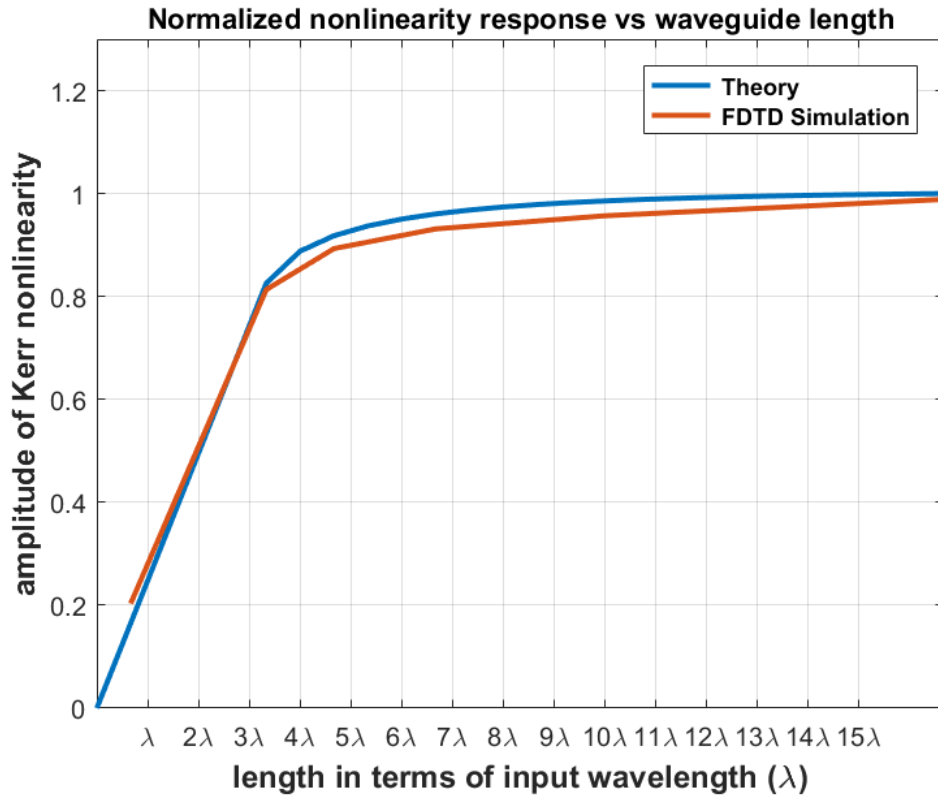
Figure 4.6: The Kerr nonlinearity amplitude of graphene integrated silicon-nitride waveguide normalized to the maximum obtained value from equation (4.4) versus different waveguide lengths obtained by FDTD simulation, and the explained theory.

4.5   Power analysis

Studying the effect of input power on the nonlinear response of this waveguide, the normalized amplitude of Kerr nonlinearity has been obtained using the simulation for different electric fields in the waveguide. Figure 4.7 shows the power analysis of Graphene integrated silicon-nitride waveguide obtained from FDTD simulation up to the breakdown voltage of silicon-nitride and graphene [58, 59].
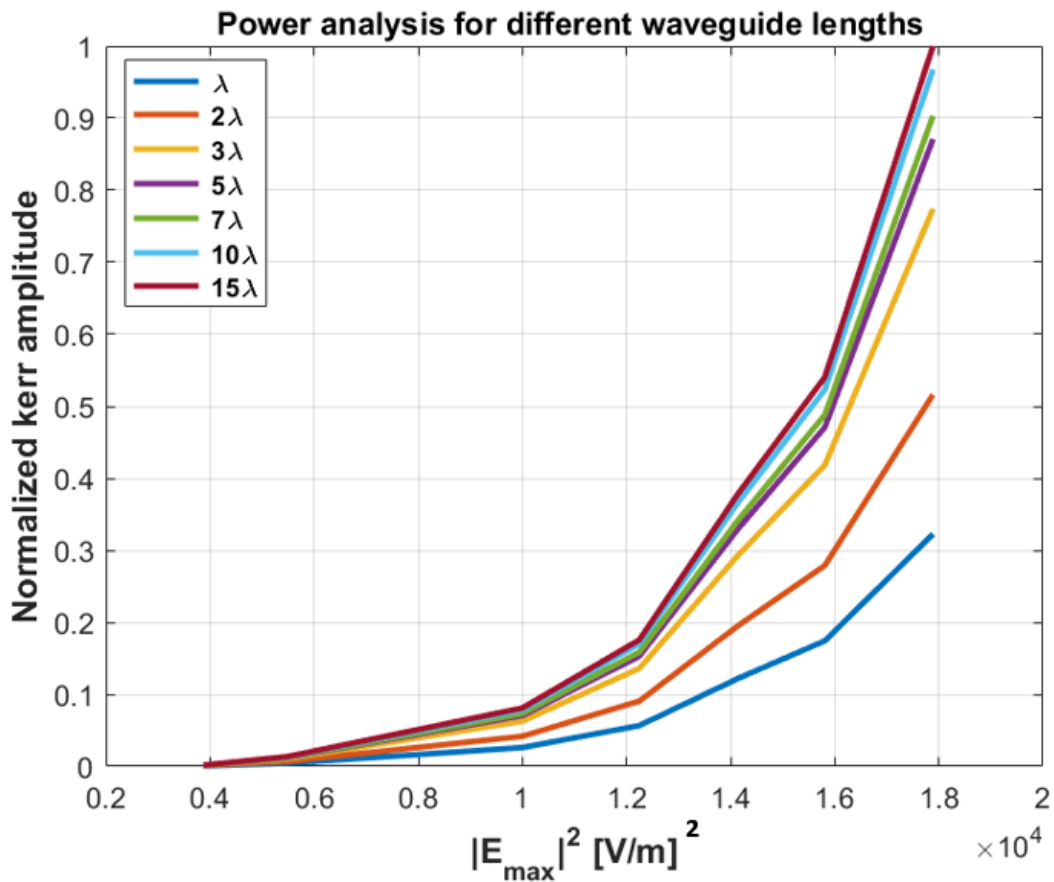
Figure 4.7: Graphene integrated silicon-nitride waveguide power analysis which is normalized to the highest achieved Kerr nonlinearity amplitude versus the maximum input electric field shown as $E(t)$ in equation (3.6) for different lengths.

The generalized nonlinear optical response can be expressed by polarization as[41]:

$$
\begin{aligned}
P(t) &= \epsilon_0 [\chi^{(1)} E(t) + \chi^{(2)} E^2(t) + \chi^{(3)} E^3(t) + ...] \\
&= P^{(1)}(t) + P^{(2)}(t) + P^{(3)}(t) + ...,
\end{aligned}
\tag{4.47}
$$

Equation (4.47) shows that the third-order nonlinear response is proportional to $\chi^{(3)} E^3(t)$, and the power analysis graph shown in Figure 4.7 follows this proportionality.

4.6 graphene integrated silicon nitride waveguide with lower cladding

As shown in section 4.3, adding a single layer of graphene can have a great impact on the nonlinear response of silicon nitride. However, the structure shown in Figure 4.4 is very hard to fabricate due to lack of substrate. Having that in mind, a low loss single-stripe silicon nitride waveguide has been used [55, 56]. In order to add a graphene layer on top of the core of this waveguide, the top cladding has to be removed. The simulation condition is same as the one we used to simulate graphene integrated silicon-nitride waveguide in section 4.3.
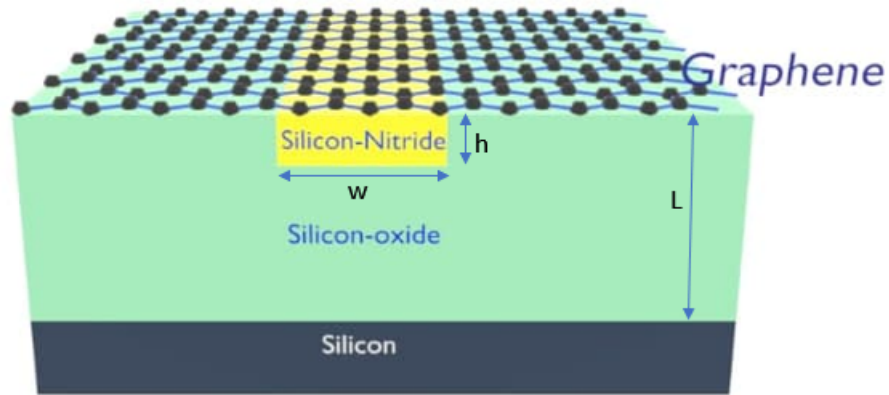
Figure 4.8: Single core silicon nitride waveguide structure, with top cladding removed and a single layer of graphene added on top of it. The dimension of this waveguide is $w = 4.2 \ \mu m$, $h = 65 \ nm$, and $L = 15 \ \mu m$, and the silicon thickness layer is $5 \ \mu m$.

Removing the top cladding makes the waveguide structure extremely asymmetric, which can result in the production of high substrate mode. To avoid this we should choose the source wavelength such that the refractive index of Silicon-oxide becomes lower than 1.2. This condition can be achieved by choosing the wavelength $6.7 \mu m$ or $20 \mu m$ for which the refractive index of silicon-oxide is 1.1596 and 1.11, respectively. The other solutions can be increasing the thickness of graphene layer up to $20 nm$ (which in this case it is called graphite), or adding a top cladding silicon-oxide layer.
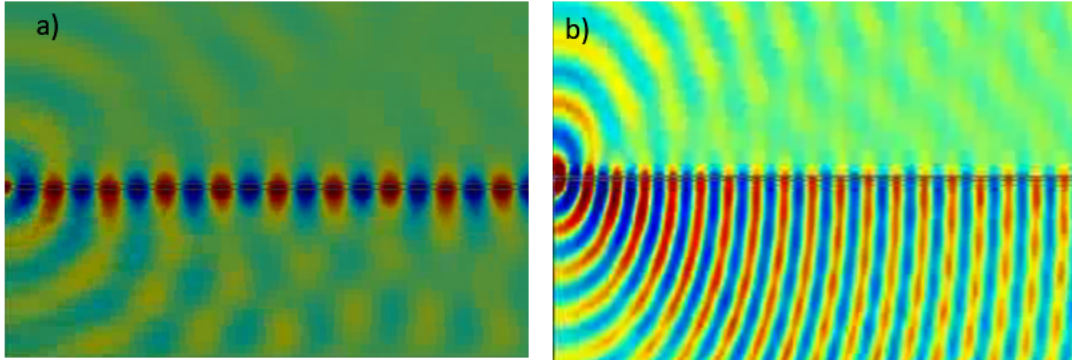
Figure 4.9: Two-dimensional wave propagation in Single-stripe silicon-nitride waveguide with no top cladding a) the wavelength of the source is $6.17\mu m$ where the refractive index of silicon-oxide is 1.16 b) high substrate mode produced when the wavelength of the source becomes $1.55\mu m$, and the structure becomes more asymmetric.

Figure 4.10 shows the length analysis of the waveguide structure, shown in figure 4.8. As the substrate mode of this structure is high, increasing the length of the waveguide results in decreasing of the electric field provided by the source inside the core. Considering equation (4.47), this reduction of electric field decreases the third-order nonlinearity response.

Normalized nonlinearity response vs waveguide length
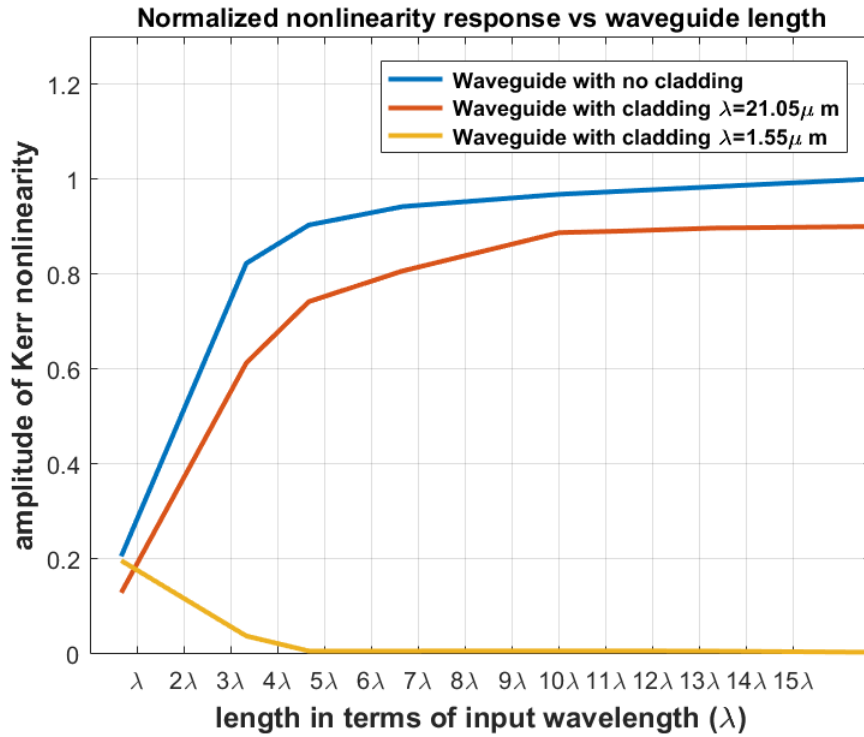
Figure 4.10: The normalized Kerr amplitude versus length for the waveguide structure shown in Figure 4.8 considering two different input wavelengths of $21.05\mu m$ and $1.55\mu m$, compared with simulation results of graphene integrated silicon-nitride waveguide shown on figure 4.6.

Figure 4.6 shows that the feasible waveguide structure shown in figure 4.10 has a great enhancement of Kerr nonlinear response in some specific wavelengths. In order to work with other wavelengths, this waveguide has a length limitation of 2λ.

Chapter 5

Conclusion

This thesis represents a simulation, analysis, and design of graphene integrated silicon-nitride waveguide. Graphene is found to be a great candidate to enhance the Kerr nonlinear response of silicon-nitride waveguide, due to its unique optical, and mechanical properties such as high third-order nonlinear response and being CMOS compatible.

The linear and nonlinear optical properties of graphene have been investigated in chapter 2. Unlike bulk materials, we used conductivity to represent the behavior of graphene, and the nonlinear conductivity of graphene is derived using the Boltzmann equation of motion.

In chapter 3 graphene has been modeled as a current sheet, and its behavior is investigated by simulating a partial graphene integrated dielectric waveguide. As a result, the graphene layer enhanced the confinement, and generated the third harmonic in the waveguide.

Owing to the high Kerr nonlinear response of graphene, the nonlinear optical response of silicon-nitride waveguide can be enhanced by as much as 7.6%, which is discussed in chapter 4. In addition, the FDTD simulation method used to model multi-layer nonlinear material is discussed in this chapter,and the nonlinear performance of graphene integrated silicon-nitride in the presence and absence of an extra silicon-oxide/silicon substrate layer is demonstrated by detailed power and length analysis. Furthermore, practical issues such as the convergence of FDTD simulation when the graphene layer is added, and the formation of substrate mode, which happens because of asymmetric structure resulted from removing the top cladding of silicon-nitride waveguide are elaborated in this chapter.

This work has focused on simulation, design and analysis of graphene integrated silicon-nitride waveguide. The next step would be the fabrication of the graphene integrated

silicon-nitride waveguide and performing an experiment to characterize the reflection and transmission measurements. Then by applying a DC voltage this structure can also be used to be an electro optical modulator as graphene has a zero-gap band structure, which is sensitive to variations of the energy potential change.

References

[1] H. L. Calvo, H. M. Pastawski, S. Roche, and L. E. F. Torres, "Tuning laser-induced band gaps in graphene," *Applied Physics Letters*, vol. 98, no. 23, p. 232103, 2011.

[2] J.-M. Liu and I.-T. Lin, *Graphene photonics.* Cambridge University Press, 2018.

[3] B. Corcoran, C. Monat, C. Grillet, D. J. Moss, B. J. Eggleton, T. P. White, L. O'Faolain, and T. F. Krauss, "Green light emission in silicon through slow-light enhanced third-harmonic generation in photonic-crystal waveguides," *Nature photonics*, vol. 3, no. 4, pp. 206–210, 2009.

[4] B. Corcoran, C. Monat, M. Pelusi, C. Grillet, T. White, L. O'Faolain, T. F. Krauss, B. J. Eggleton, and D. J. Moss, "Optical signal processing on a silicon chip at 640gb/s using slow-light," *Optics express*, vol. 18, no. 8, pp. 7770–7781, 2010.

[5] J. S. Levy, A. Gondarenko, M. A. Foster, A. C. Turner-Foster, A. L. Gaeta, and M. Lipson, "Cmos-compatible multiple-wavelength oscillator for on-chip optical interconnects," *Nature photonics*, vol. 4, no. 1, pp. 37–40, 2010.

[6] L. Razzari, D. Duchesne, M. Ferrera, R. Morandotti, S. Chu, B. Little, and D. Moss, "Cmos-compatible integrated optical hyper-parametric oscillator," *Nature Photonics*, vol. 4, no. 1, pp. 41–45, 2010.

[7] C. Koos, P. Vorreau, T. Vallaitis, P. Dumon, W. Bogaerts, R. Baets, B. Esembeson, I. Biaggio, T. Michinobu, F. Diederich, *et al.*, "All-optical high-speed signal processing with silicon–organic hybrid slot waveguides," *Nature photonics*, vol. 3, no. 4, pp. 216–219, 2009.

[8] H. Ji, M. Pu, H. Hu, M. Galili, L. K. Oxenlowe, K. Yvind, J. M. Hvam, and P. Jeppesen, "Optical waveform sampling and error-free demultiplexing of 1.28 tb/s serial data in a nanoengineered silicon waveguide," *Journal of Lightwave Technology*, vol. 29, no. 4, pp. 426–431, 2010.

[9] M. A. Foster, A. C. Turner, J. E. Sharping, B. S. Schmidt, M. Lipson, and A. L. Gaeta, "Broad-band optical parametric gain on a silicon photonic chip," *Nature*, vol. 441, no. 7096, pp. 960–963, 2006.

[10] M. A. Foster, A. C. Turner, R. Salem, M. Lipson, and A. L. Gaeta, "Broad-band continuous-wave parametric wavelength conversion in silicon nanowaveguides," *Optics Express*, vol. 15, no. 20, pp. 12949–12958, 2007.

[11] M. Kues, C. Reimer, P. Roztocki, L. R. Cortés, S. Sciara, B. Wetzel, Y. Zhang, A. Cino, S. T. Chu, B. E. Little, *et al.*, "On-chip generation of high-dimensional entangled quantum states and their coherent control," *Nature*, vol. 546, no. 7660, pp. 622–626, 2017.

[12] C. Reimer, M. Kues, P. Roztocki, B. Wetzel, F. Grazioso, B. E. Little, S. T. Chu, T. Johnston, Y. Bromberg, L. Caspani, *et al.*, "Generation of multiphoton entangled quantum states by means of integrated frequency combs," *Science*, vol. 351, no. 6278, pp. 1176–1180, 2016.

[13] M. A. Foster, R. Salem, D. F. Geraghty, A. C. Turner-Foster, M. Lipson, and A. L. Gaeta, "Silicon-chip-based ultrafast optical oscilloscope," *Nature*, vol. 456, no. 7218, pp. 81–84, 2008.

[14] J. Leuthold, C. Koos, and W. Freude, "Nonlinear silicon photonics," *Nature photonics*, vol. 4, no. 8, pp. 535–544, 2010.

[15] D. J. Moss, R. Morandotti, A. L. Gaeta, and M. Lipson, "New cmos-compatible platforms based on silicon nitride and hydex for nonlinear optics," *Nature photonics*, vol. 7, no. 8, pp. 597–607, 2013.

[16] R. Salem, M. A. Foster, A. C. Turner, D. F. Geraghty, M. Lipson, and A. L. Gaeta, "Signal regeneration using low-power four-wave mixing on silicon chip," *Nature photonics*, vol. 2, no. 1, pp. 35–38, 2008.

[17] P. Dong, Y.-K. Chen, G.-H. Duan, and D. T. Neilson, "Silicon photonic devices and integrated circuits," *Nanophotonics*, vol. 3, no. 4-5, pp. 215–228, 2014.

[18] A. D. Bristow, N. Rotenberg, and H. M. Van Driel, "Two-photon absorption and kerr coefficients of silicon for 850–2200 nm," *Applied Physics Letters*, vol. 90, no. 19, p. 191104, 2007.

[19] R. Wu, Y. Zhang, S. Yan, F. Bian, W. Wang, X. Bai, X. Lu, J. Zhao, and E. Wang, "Purely coherent nonlinear optical response in solution dispersions of graphene sheets," *Nano letters*, vol. 11, no. 12, pp. 5159–5164, 2011.

[20] S. Thakur, B. Semnani, and A. H. Majedi, "Spectrally-dependent z-scan measurement of the nonlinear refractive index of graphene," in *2017 Photonics North (PN)*, pp. 1–2, IEEE, 2017.

[21] S. Thakur, B. Semnani, S. Safavi-Naeini, and A. H. Majedi, "Experimental characterization of the ultrafast, tunable and broadband optical kerr nonlinearity in graphene," *Scientific reports*, vol. 9, no. 1, pp. 1–10, 2019.

[22] M. I. Katsnelson and M. I. Katsnelson, *Graphene: carbon in two dimensions*. Cambridge university press, 2012.

[23] M. L. Nesterov, J. Bravo-Abad, A. Y. Nikitin, F. J. García-Vidal, and L. Martin-Moreno, "Graphene supports the propagation of subwavelength optical solitons," *Laser & Photonics Reviews*, vol. 7, no. 2, pp. L7–L11, 2013.

[24] M. Qasymeh and H. Eleuch, "Hybrid two-mode squeezing of microwave and optical fields using optically pumped graphene layers," *Scientific reports*, vol. 10, no. 1, pp. 1–10, 2020.

[25] M. Liu, X. Yin, E. Ulin-Avila, B. Geng, T. Zentgraf, L. Ju, F. Wang, and X. Zhang, "A graphene-based broadband optical modulator," *Nature*, vol. 474, no. 7349, pp. 64–67, 2011.

[26] C. e. e. Rao, A. e. Sood, K. e. Subrahmanyam, and A. Govindaraj, "Graphene: the new two-dimensional nanomaterial," *Angewandte Chemie International Edition*, vol. 48, no. 42, pp. 7752–7777, 2009.

[27] M. Y. Han, B. Özyilmaz, Y. Zhang, and P. Kim, "Energy band-gap engineering of graphene nanoribbons," *Physical review letters*, vol. 98, no. 20, p. 206805, 2007.

[28] B. Sensale-Rodriguez, R. Yan, M. M. Kelly, T. Fang, K. Tahy, W. S. Hwang, D. Jena, L. Liu, and H. G. Xing, "Broadband graphene terahertz modulators enabled by intraband transitions," *Nature communications*, vol. 3, no. 1, pp. 1–7, 2012.

[29] K. L. Ishikawa, "Nonlinear optical response of graphene in time domain," *Physical Review B*, vol. 82, no. 20, p. 201402, 2010.

[30] K. F. Mak, L. Ju, F. Wang, and T. F. Heinz, "Optical spectroscopy of graphene: From the far infrared to the ultraviolet," *Solid State Communications*, vol. 152, no. 15, pp. 1341–1349, 2012.

[31] F. Wang, Y. Zhang, C. Tian, C. Girit, A. Zettl, M. Crommie, and Y. R. Shen, "Gate-variable optical transitions in graphene," *science*, vol. 320, no. 5873, pp. 206–209, 2008.

[32] L. Yang, J. Deslippe, C.-H. Park, M. L. Cohen, and S. G. Louie, "Excitonic effects on the optical response of graphene and bilayer graphene," *Physical review letters*, vol. 103, no. 18, p. 186802, 2009.

[33] Q. Bao, H. Zhang, Y. Wang, Z. Ni, Y. Yan, Z. X. Shen, K. P. Loh, and D. Y. Tang, "Atomic-layer graphene as a saturable absorber for ultrafast pulsed lasers," *Advanced Functional Materials*, vol. 19, no. 19, pp. 3077–3083, 2009.

[34] D. B. Davidson, *Computational electromagnetics for RF and microwave engineering.* Cambridge University Press, 2010.

[35] T. M. Habashy, M. L. Oristaglio, and A. T. de Hoop, "Simultaneous nonlinear reconstruction of two-dimensional permittivity and conductivity," *Radio Science*, vol. 29, no. 4, pp. 1101–1118, 1994.

[36] J.-M. Jin, *Theory and computation of electromagnetic fields.* John Wiley & Sons, 2011.

[37] A. Taflove, A. Oskooi, and S. G. Johnson, *Advances in FDTD computational electro-dynamics: photonics and nanotechnology.* Artech house, 2013.

[38] G. W. Hanson, "Dyadic green's functions for an anisotropic, non-local model of biased graphene," *IEEE Transactions on antennas and propagation*, vol. 56, no. 3, pp. 747–757, 2008.

[39] H. Hajian, A. Soltani-Vala, M. Kalafi, and P. T. Leung, "Surface plasmons of a graphene parallel plate waveguide bounded by kerr-type nonlinear media," *Journal of Applied Physics*, vol. 115, no. 8, p. 083104, 2014.

[40] L. Falkovsky, "Optical properties of graphene," in *Journal of Physics: conference series*, vol. 129, p. 012004, IOP Publishing, 2008.

[41] R. W. Boyd, *Nonlinear optics.* Academic press, 2020.

[42] S. A. Mikhailov, "Non-linear electromagnetic response of graphene," *EPL (Europhysics Letters)*, vol. 79, no. 2, p. 27002, 2007.

[43] J. Wang, Y. Hernandez, M. Lotya, J. N. Coleman, and W. J. Blau, "Broadband nonlinear optical response of graphene dispersions," *Advanced Materials*, vol. 21, no. 23, pp. 2430–2435, 2009.

[44] M. Feng, H. Zhan, and Y. Chen, "Nonlinear optical and optical limiting properties of graphene families," *Applied Physics Letters*, vol. 96, no. 3, p. 033107, 2010.

[45] N. Liaros, A. Bourlinos, R. Zboril, and S. Couris, "Fluoro-graphene: nonlinear optical properties," *Optics express*, vol. 21, no. 18, pp. 21027–21038, 2013.

[46] E. Dremetsika, B. Dlubak, S.-P. Gorza, C. Ciret, M.-B. Martin, S. Hofmann, P. Seneor, D. Dolfi, S. Massar, P. Emplit, *et al.*, "Measuring the nonlinear refractive index of graphene using the optical kerr effect method," *Optics Letters*, vol. 41, no. 14, pp. 3281–3284, 2016.

[47] N. Vermeulen, D. Castelló-Lurbe, J. Cheng, I. Pasternak, A. Krajewska, T. Ciuk, W. Strupinski, H. Thienpont, and J. Van Erps, "Negative kerr nonlinearity of graphene as seen via chirped-pulse-pumped self-phase modulation," *Physical Review Applied*, vol. 6, no. 4, p. 044006, 2016.

[48] C. Q. Xia, C. Zheng, M. S. Fuhrer, and S. Palomba, "Nonlinear optical frequency mixing response of single and multilayer graphene," *Optics Letters*, vol. 41, no. 6, pp. 1122–1125, 2016.

[49] H. Nasari and M. S. Abrishamian, "All-optical tunable notch filter by use of kerr nonlinearity in the graphene microribbon array," *JOSA B*, vol. 31, no. 7, pp. 1691–1697, 2014.

[50] J. G. Proakis and M. Salehi, *Fundamentals of communication systems*. Pearson Education India, 2007.

[51] J. K. Wassei and R. B. Kaner, "Graphene, a promising transparent conductor," *Materials today*, vol. 13, no. 3, pp. 52–59, 2010.

[52] K. S. Kunz and R. J. Luebbers, *The finite difference time domain method for electromagnetics*. CRC press, 1993.

[53] H. Nasari and M. Abrishamian, "Electrically tunable, plasmon resonance enhanced, terahertz third harmonic generation via graphene," *RSC advances*, vol. 6, no. 55, pp. 50190–50200, 2016.

[54] K. Ikeda, R. E. Saperstein, N. Alic, and Y. Fainman, "Thermal and kerr nonlinear properties of plasma-deposited silicon nitride/silicon dioxide waveguides," *Optics express*, vol. 16, no. 17, pp. 12987–12994, 2008.

[55] C. G. Roeloffzen, M. Hoekman, E. J. Klein, L. S. Wevers, R. B. Timens, D. Marchenko, D. Geskus, R. Dekker, A. Alippi, R. Grootjans, *et al.*, "Low-loss si3n4 triplex optical waveguides: Technology and applications overview," *IEEE journal of selected topics in quantum electronics*, vol. 24, no. 4, pp. 1–21, 2018.

[56] J. F. Bauters, M. J. Heck, D. D. John, M.-C. Tien, W. Li, J. S. Barton, D. J. Blumenthal, J. E. Bowers, A. Leinse, and R. G. Heideman, "Ultra-low-loss single-mode si3n4 waveguides with 0.7 db/m propagation loss," in *European Conference and Exposition on Optical Communications*, pp. Th–12, Optical Society of America, 2011.

[57] S. Romero-García, F. Merget, F. Zhong, H. Finkelstein, and J. Witzens, "Silicon nitride cmos-compatible platform for integrated photonics applications at visible wavelengths," *Optics express*, vol. 21, no. 12, pp. 14036–14046, 2013.

[58] X. Yan, I. S. Esqueda, J. Ma, J. Tice, and H. Wang, "High breakdown electric field in β-ga2o3/graphene vertical barristor heterostructure," *Applied Physics Letters*, vol. 112, no. 3, p. 032101, 2018.

[59] C. Rauthan and J. Srivastava, "Electrical breakdown voltage characteristics of buried silicon nitride layers and their correlation to defects in the nitride layer," *Materials Letters*, vol. 9, no. 7-8, pp. 252–258, 1990.

[60] B. Semnani, "Graphene-assisted integrated nonlinear optics," 2018.

[61] K. Kristinsson, O. V. Kibis, S. Morina, and I. A. Shelykh, "Control of electronic transport in graphene by electromagnetic dressing," *Scientific reports*, vol. 6, no. 1, pp. 1–7, 2016.

[62] S. A. Mikhailov and K. Ziegler, "New electromagnetic mode in graphene," *Physical review letters*, vol. 99, no. 1, p. 016803, 2007.

[63] J.-L. Cheng, N. Vermeulen, and J. Sipe, "Third order optical nonlinearity of graphene," *New Journal of Physics*, vol. 16, no. 5, p. 053014, 2014.

[64] Z. Liu, Y. Wang, X. Zhang, Y. Xu, Y. Chen, and J. Tian, "Nonlinear optical properties of graphene oxide in nanosecond and picosecond regimes," *Applied Physics Letters*, vol. 94, no. 2, p. 021902, 2009.

[65] Z.-B. Liu, Y.-F. Xu, X.-Y. Zhang, X.-L. Zhang, Y.-S. Chen, and J.-G. Tian, "Porphyrin and fullerene covalently functionalized graphene hybrid materials with large nonlinear optical properties," *The Journal of Physical Chemistry B*, vol. 113, no. 29, pp. 9681–9686, 2009.

[66] S. A. Mikhailov and K. Ziegler, "Nonlinear electromagnetic response of graphene: frequency multiplication and the self-consistent-field effects," *Journal of Physics: Condensed Matter*, vol. 20, no. 38, p. 384204, 2008.

[67] D. J. Griffiths and D. F. Schroeter, *Introduction to quantum mechanics.* Cambridge University Press, 2018.

[68] A. Pasquazi, M. Peccianti, Y. Park, B. E. Little, S. T. Chu, R. Morandotti, J. Azaña, and D. J. Moss, "Sub-picosecond phase-sensitive optical pulse characterization on a chip," *Nature Photonics*, vol. 5, no. 10, pp. 618–623, 2011.

[69] J. Wu, X. Xu, T. G. Nguyen, S. T. Chu, B. E. Little, R. Morandotti, A. Mitchell, and D. J. Moss, "Rf photonics: an optical microcombs' perspective," *IEEE Journal of Selected Topics in Quantum Electronics*, vol. 24, no. 4, pp. 1–20, 2018.

[70] B. Zhu, G. Ren, S. Zheng, Z. Lin, and S. Jian, "Nanoscale dielectric-graphene-dielectric tunable infrared waveguide with ultrahigh refractive indices," *Optics express*, vol. 21, no. 14, pp. 17089–17096, 2013.

APPENDICES

Appendix A

Linear dispersion diagram

A.1   Mode Parameters

We can calculate the propagation constant using two different approaches. First, we calculate the propagation constant using mode parameters method.
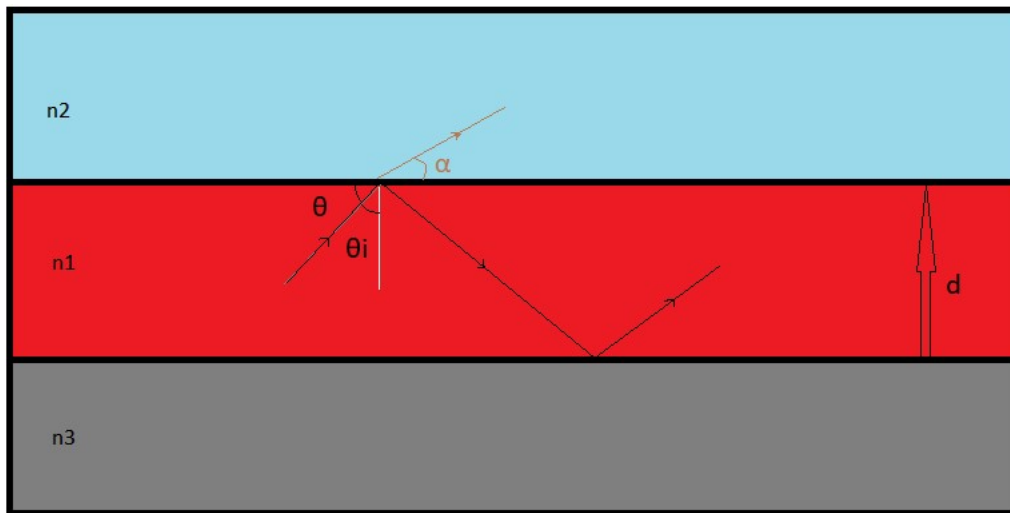

Figure A.1: Dielectric waveguide with three layers. θ_i is the incident angel, d is the thickness of the core, and α is the angel inside the top cladding.

The normalized frequency and waveguide thickness will be:

$$V = \frac{2\pi}{\lambda} d\sqrt{n_1^2 - n_3^2} = \frac{\omega}{c} d\sqrt{n_1^2 - n_3^2}, \tag{A.1}$$

And the normalized guide index is a function of propagation constant:

$$b = \frac{\beta^2 - k_3^2}{k_1^2 - k_3^2} = \frac{n_\beta^2 - n_3^2}{n_1^2 - n_3^2}, \tag{A.2}$$

where $n_\beta = \frac{\beta\lambda}{2\pi}$ is the effective refractive index of the waveguide mode that is propagation constant is β. asymmetry factor, which is a function of polarization of the mode under consideration for TE mode can be written as:

$$a_E = \frac{n_3^2 - n_2^2}{n_1^2 - n_3^2}. \tag{A.3}$$

For a guided mode, we have condition such that, $k_1 > \beta > k_3 > k_2$.

$$k_1^2 - \beta^2 = h_1^2 \tag{A.4}$$
$$\beta^2 - k_3^2 = \gamma_3^2 \tag{A.5}$$
$$\beta^3 - k_2^2 = \gamma_2^2 \tag{A.6}$$

In mentioned above condition, there should be a real value of h_1, γ_2, and γ_3 should exist.

As we know For TE mode of a planer waveguide , Maxwell's equations may be reduced to:

$$\frac{\partial^2 E_y}{\partial x^2} + (k^2 - \beta^2)E_y = 0 \tag{A.7}$$

Where $k^2 = \omega^2 \mu_0 \epsilon(x)$

Solving equation (A.7), we get:

$$E_y = C_{TE}cos(h_1 d/2 - \psi)e^{\gamma_3(d/2-x)}, x > d/2 \tag{A.8}$$
$$E_y = C_{TE}cos(h_1 d/2 - \psi), -d/2 < x < d/2$$

$$E_y = C_{TE}cos(h_1 d/2 + \psi)e^{\gamma_2(d/2-x)}, x < -d/2$$

51

And below eigenvalue equations:

$$tan(h_1 d) = \frac{h_1(\gamma_2 + \gamma_3)}{h_1^2 - \gamma_2 \gamma_3} \tag{A.9}$$

$$tan(2\psi) = \frac{h_1(\gamma_2 - \gamma_3)}{h_1^2 + \gamma_2 \gamma_3} \tag{A.10}$$

Where for normalizing the mode field, we should apply below normalization relation:

$$C_{TE} = \sqrt{\frac{\omega \mu_0}{\beta d_E}} \tag{A.11}$$

where d_E is the effective waveguide thickens:

$$d_e = d + \frac{1}{\gamma_2} + \frac{1}{\gamma_3} \tag{A.12}$$

In case of TM mode, we have:

$$H_y = C_{TM} cos(h_1 d/2 - \psi) e^{\gamma_3(d/2-x)}, x > d/2 \tag{A.13}$$
$$H_y = C_{TM} cos(h_1 d/2 - \psi), -d/2 < x < d/2$$

$$H_y = C_{TM} cos(h_1 d/2 + \psi) e^{\gamma_2(d/2-x)}, x < -d/2$$

And below eigenvalue equations:

$$tan(h_1 d) = \frac{(h_1/n_1^2)(\gamma_2/n_2^2 + \gamma_3/n_3^2)}{(h_1/n_1^2)^2 - \gamma_2 \gamma_3/n_2^2 n_3^2} \tag{A.14}$$

$$tan(2\psi) = \frac{(h_1/n_1^2)(\gamma_2/n_2^2 + \gamma_3/n_3^2)}{(h_1/n_1^2)^2 + \gamma_2 \gamma_3/n_2^2 n_3^2} \tag{A.15}$$

Where for normalizing the mode field, we should apply below normalization relation:

$$C_{TM} = \sqrt{\frac{\omega \mu_0 n_1^2}{\beta d_M}} \tag{A.16}$$

52

where d_E is the effective waveguide thickens:

$$d_M = d + \frac{1}{\gamma_2 q_2} + \frac{1}{\gamma_3 q_3} \tag{A.17}$$

Where:

$$q_2 = \frac{\beta^2}{k_1^2} + \frac{\beta^2}{k_2^2} - 1 \tag{A.18}$$

$$q_2 = \frac{\beta^2}{k_1^2} + \frac{\beta^2}{k_3^2} - 1 \tag{A.19}$$

From Equation (A.4), (A.6), and (A.5) we realize the γ_2 and γ_3 may be in terms of β and h_1. In terms of normalized waveguide parameters, we have:

$$\gamma_2^2 d^2 = \beta^2 d^2 - k_2^2 d^2 = (1 + a_E)V^2 - h_1^2 d^2 \tag{A.20}$$

$$\gamma_3^2 d^2 = \beta^2 d^2 - k_3^2 d^2 = V^2 - h_1^2 d^2 \tag{A.21}$$

As mentioned before, all discrete allowed values of propagation constant can be assumed only on one independent variable h_1, which can be determined by solving equation (A.9). For our considered waveguide, we have $d = 1\mu m$, $n_3 = 1.2$, $n_1 = 1.5$, and $n_2 = 1$.

As a result, using a new variable $\zeta = h_1 d$ the mentioned eigenvalue equations for TE and TM mode can be written as:

$$tan(\zeta) = \zeta \frac{\sqrt{V^2 - \zeta^2} + \sqrt{(1 + a_E)V^2 - \zeta^2}}{\zeta^2 - \sqrt{V^2 - \zeta^2}\sqrt{(1 + a_E)V^2 - \zeta^2}}(TE) \tag{A.22}$$

$$tan(\zeta) = \zeta \frac{n_1^2 n_2^2 \sqrt{V^2 - \zeta^2} + n_1^2 n_3^2 \sqrt{(1 + a_E)V^2 - \zeta^2}}{n_2^2 n_3^2 \zeta^2 - n_1^4 \sqrt{V^2 - \zeta^2}\sqrt{(1 + a_E)V^2 - \zeta^2}}(TM) \tag{A.23}$$

A.2   Self-Consistency Method

Using the transmission line model, we may calculate the calculate the reflection coefficient and the phase change.

$$R = \frac{\eta_2 - \eta_1}{\eta_2 + \eta_1} = \frac{\frac{1}{n_2 sin(\alpha)} - \frac{1}{n_1 sin(\theta)}}{\frac{1}{n_2 sin(\alpha)} + \frac{1}{n_1 sin(\theta)}} \qquad (A.24)$$

Considering total internal reflection, we have: $sin(\alpha) = -J\sqrt{(\frac{n_1}{n_1})^2 cos^2(\theta) - 1}$. As a result, equation (A.24) reads:

$$R = \frac{\frac{-1}{n_1 sin(\theta)} + J\frac{1}{n_2\sqrt{(\frac{n_1}{n_2})^2 cos^2(\theta) - 1}}}{\frac{1}{n_1 sin(\theta)} + J\frac{1}{n_2\sqrt{(\frac{n_1}{n_2})^2 cos^2(\theta) - 1}}} \qquad (A.25)$$

The phase change of total internal reflection will be:

$$\Delta\phi = \pi - 2tan^{-1}(\frac{n_1 sin(\theta)}{n_2\sqrt{(\frac{n_1}{n_2})^2 cos^2(\theta) - 1}}) \qquad (A.26)$$

Using $tan^{-1}(x) + tan^{-1}(\frac{1}{x}) = \frac{\pi}{2}$ equation (A.26) reads:

$$\Delta\phi = 2tan^{-1}(\frac{n_2\sqrt{(\frac{n_1}{n_2})^2 cos^2(\theta) - 1}}{n_1 sin(\theta)}) \qquad (A.27)$$

Using the propagation constant $\beta = k_0 n_1 cos(\theta)$ equation (A.27) reads :

$$\Delta\phi = 2tan^{-1}(\frac{\sqrt{\beta^2 - k_0^2 n_2^2}}{\sqrt{k_0^2 n_1^2 - \beta^2}}) \qquad (A.28)$$

For self-consistency the whole phase shift has to be $m*2\pi$ where $m = 1, 2, 3, ...$ shows the mode number. The whole phase shift will be:

$$\Delta\phi_1 + \Delta\phi_2 - 2\sqrt{k_0^2 n_1^2 + \beta^2}d = 2m\pi \qquad (A.29)$$

Where $\Delta\phi_1$ and $\Delta\phi_2$ are the phase shift introduced by upper and lower cladding reflection respectively. The term $2\sqrt{k_0^2 n_1^2 - \beta^2}$ shows the phase shift caused by travelling distance inside the waveguide.

$$2tan^{-1}(\frac{\sqrt{\beta^2 - k_0^2 n_2^2}}{\sqrt{k_0^2 n_1^2 - \beta^2}}) + 2tan^{-1}(\frac{\sqrt{\beta^2 - k_0^2 n_3^2}}{\sqrt{k_0^2 n_1^2 - \beta^2}}) - 2\sqrt{k_0^2 n_1^2 - \beta^2}d = 2m\pi \qquad (A.30)$$

$$tan^{-1}(\frac{\sqrt{\beta^2 - k_2^2}}{\sqrt{k_1^2 - \beta^2}}) + tan^{-1}(\frac{\sqrt{\beta^2 - k_3^2}}{\sqrt{k_1^2 - \beta^2}}) - \sqrt{k_1^2 - \beta^2}d = m\pi \qquad (A.31)$$

To see the number of modes inside the waveguide, we plot the left hand side of equation (A.31) in respect to valid values of beta. By valid values of we mean the values which makes square roots of equation (A.31) positive values.
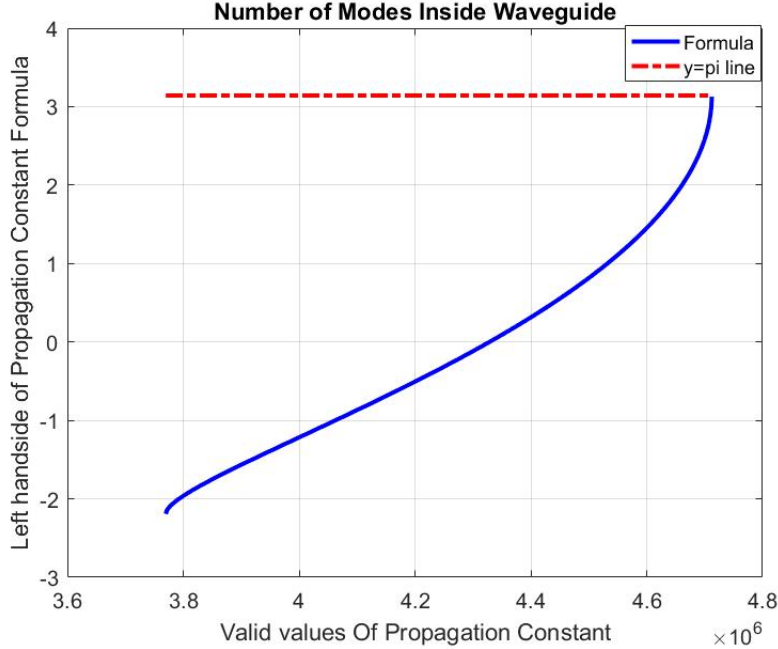

Figure A.2: The left and right hand side of equation (A.31) for checking possible mode (valid values of m). As can be seen we get just the first mode as our answer

Using the relation between guided wavelength and propagation constant shown in equation (A.32) we may calculate propagation constant from our FDTD simulation. It is worth mention that both methods will give you exact same results, because basically you may derive one from other.

$$\beta = \frac{2\pi}{\lambda_g} \tag{A.32}$$

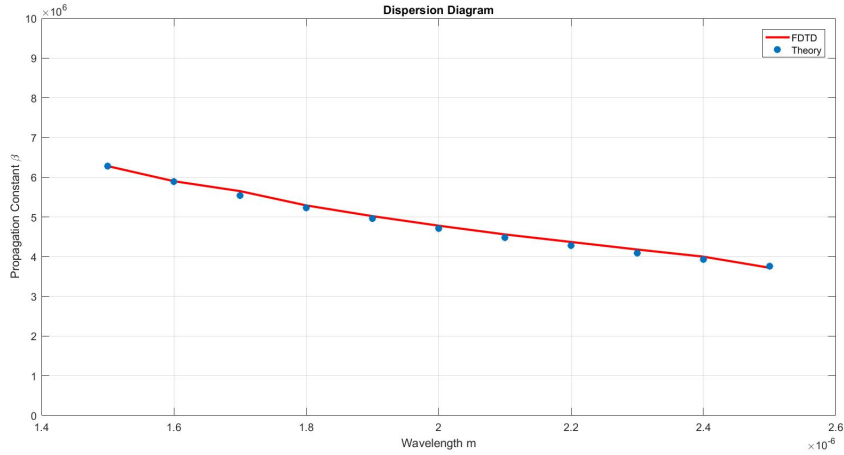Figure A.3 shows the dispersion diagram, obtained from theory and FDTD method.

Figure A.3: dispersion diagram obtained from theory and FDTD method

the difference seen in this graph raises from the fact that, the guided wavelength is calculated mesh difference of two peak values multiplied by spatial difference which is in the order of micrometer. As a result, less tan one mesh difference may cause considerable difference compared to theory solution.